

PAPER • OPEN ACCESS

High resolution stereolithography fabrication of perfusable scaffolds to enable long-term meso-scale hepatic culture for disease modeling

To cite this article: Pierre Sphabmixay *et al* 2021 *Biofabrication* **13** 045024

View the [article online](#) for updates and enhancements.

You may also like

- [Search for Gravitational Waves Associated with Gamma-Ray Bursts Detected by Fermi and Swift during the LIGO–Virgo Run O3b](#)
R. Abbott, T. D. Abbott, F. Acernese et al.
- [Narrowband Searches for Continuous and Long-duration Transient Gravitational Waves from Known Pulsars in the LIGO–Virgo Third Observing Run](#)
R. Abbott, T. D. Abbott, F. Acernese et al.
- [Emission measurements from planar arrays of porous ionic liquid ion sources](#)
Daniel G Courtney, Hanqing Q Li and Paulo Lozano



Breath Biopsy[®] OMNI

The most advanced, complete solution for global breath biomarker analysis

SEE WHAT OMNI
CAN DO FOR YOU



Expert Study Design
& Management



Robust Breath
Collection



Reliable Sample
Processing & Analysis



In-depth Data
Analysis



Specialist Data
Interpretation

Biofabrication



PAPER

OPEN ACCESS

RECEIVED
11 May 2021

REVISED
18 August 2021

ACCEPTED FOR PUBLICATION
3 September 2021

PUBLISHED
21 September 2021

Original content from this work may be used under the terms of the [Creative Commons Attribution 4.0 licence](#).

Any further distribution of this work must maintain attribution to the author(s) and the title of the work, journal citation and DOI.



High resolution stereolithography fabrication of perfusable scaffolds to enable long-term meso-scale hepatic culture for disease modeling

Pierre Sphabmixay^{1,2} , Micha Sam Brickman Raredon^{3,4} , Alex J-S Wang⁵ , Howon Lee⁶ , Paula T Hammond^{7,8} , Nicholas X Fang¹ and Linda G Griffith^{1,5,9,*}

¹ Department of Mechanical Engineering, Massachusetts Institute of Technology, Cambridge, MA, United States of America

² Whitehead Institute of Biomedical Research, Massachusetts Institute of Technology, Cambridge, MA, United States of America

³ Department of Biomedical Engineering, Yale University, New Haven, CT, United States of America

⁴ Vascular Biology and Therapeutics, Yale University, New Haven, CT, United States of America

⁵ Department of Biological Engineering, Massachusetts Institute of Technology, Cambridge, MA, United States of America

⁶ Department of Mechanical Engineering, Seoul National University, Seoul, Korea

⁷ Department of Chemical Engineering, Massachusetts Institute of Technology, Cambridge, MA, United States of America

⁸ Koch Institute for Integrative Cancer Research, Massachusetts Institute of Technology, Cambridge, MA, United States of America

⁹ Center for Gynecopathology Research, Massachusetts Institute of Technology, Cambridge, MA, United States of America

* Author to whom any correspondence should be addressed.

E-mail: griff@mit.edu

Keywords: mesoscale, perfusion, hepatocytes, projection micro-stereolithography, oxygen, shear stress, insulin resistance

Supplementary material for this article is available [online](#)

Abstract

Microphysiological systems (MPS), comprising human cell cultured in formats that capture features of the three-dimensional (3D) microenvironments of native human organs under microperfusion, are promising tools for biomedical research. Here we report the development of a mesoscale physiological system (MePS) enabling the long-term 3D perfused culture of primary human hepatocytes at scales of over 10^6 cells per MPS. A central feature of the MePS, which employs a commercially-available multiwell bioreactor for perfusion, is a novel scaffold comprising a dense network of nano- and micro-porous polymer channels, designed to provide appropriate convective and diffusive mass transfer of oxygen and other nutrients while maintaining physiological values of shear stress. The scaffold design is realized by a high resolution stereolithography fabrication process employing a novel resin. This new culture system sustains mesoscopic hepatic tissue-like cultures with greater hepatic functionality (assessed by albumin and urea synthesis, and CYP3A4 activity) and lower inflammation markers compared to comparable cultures on the commercial polystyrene scaffold. To illustrate applications to disease modeling, we established an insulin-resistant phenotype by exposing liver cells to hyperglycemic and hyperinsulinemic media. Future applications of the MePS include the co-culture of hepatocytes with resident immune cells and the integration with multiple organs to model complex liver-associated diseases

1. Introduction

Over the past few decades, integration of engineering and life sciences have led to the development of three-dimensional (3D) culturing methods allowing for the creation of organ-like systems, also known as organ-on-chip (OOC) or microphysiological systems (MPS) [1]. While biomedical research

has made groundbreaking advances using traditional static two-dimensional (2D) culture methods, which offer benefits such as simplicity, throughput and reproducibility, researchers have been confronted with mounting evidence that 2D culture on hard plastics lacks physiological translatability when comparing *in vitro* outcomes with *in vivo* data [2]. These observations have fueled the efforts to create

'MicroPhysiological Systems' (MPS) that better capture complex 3D features of human tissues [3, 4] for applications in toxicology, pharmacokinetics, and disease modeling [4]. Currently, animals are still the benchmark validation models before human clinical trials for medical regulators. However, animal models often fail to appropriately recapitulate human physiology due to major inter-species differences [5] in biological pathways, metabolism, genetic variations and pharmacodynamics.

Although MPS approaches have been applied to almost every organ of the human body [6–14] there is still no consensus on how MPS should be scaled for research or drug development purposes. Optimal values of fundamental parameters of the MPS construction and operation, such as the number of cells, the volume of media, flow rate, surface area, or concentration of biochemicals, are dictated by the particular applications of each MPS, with predictive models for human responses still emerging [15]. Consideration of scaling parameters is particularly crucial when considering interconnecting several organs together—for example, in the long term culture of ten MPS at a time on a single human-on-chip platform [16] and in more focused studies with 2–4 MPSs [9, 17, 18]. As the cells comprising MPS are typically an expensive commodity, a preponderance of MPS designs emphasize miniaturization to operate at micrometric scale with relatively few cells, which can often lead to an overwhelmingly skewed cell/media ratio, thus diluting autocrine factors and inhibiting depletion or accumulation of critical biochemicals in the circulating media [19–21]. Further, while some optical or molecular assays are compatible with 10^3 – 10^5 cells, assays ranging from detailed transcriptional analyses to mass spectrometry or phosphoproteomics may require 10^6 – 10^8 cells [15, 19]. Similarly, disease modeling such as tumor metastases in a host tissue may require substantial cell mass to replicate phenomena adequately [15, 20, 21]. These observations motivate the need to design physiological systems at mesoscopic scale between micrometric MPS and macrometric animal models, which would help bridge the gap between the two fields and provide more physiologically relevant *in vitro* models.

An essential feature for the 3D culture of human cells in OOC is providing nutrients and oxygen deep into the tissue while removing waste products [10]. This function, performed *in vivo* by a dense vasculature network, has driven efforts to recreate perfusable microfluidic networks *in vitro*, especially for cells exhibiting elevated metabolic rates such as primary human liver cells [22, 23] with a diffusion length of oxygen on the order of 50–100 μm s [24, 25]. As a result, most liver MPS designs have focused on relatively small cell numbers and dimension [26–31]

and implementation has relied heavily on microfabrication techniques capable of working at such small scales [32]. The difficulty of culturing primary human hepatocytes (PHH) in 3D may be linked to the exceptional range of vital biological functions that the liver fulfills, serving as the nexus for more than 500 functions [33], including detoxification, protein synthesis for blood plasma, and metabolism of lipids and carbohydrates. As a result, the liver is the second-most oxygen-consuming organ of the human body after the brain [34], which is reflected *in vitro* by the need to perfuse liver OOC at elevated flow rates compared to other organs. Hollow fiber bioreactor designs adapted from clinical extracorporeal liver support applications, and scaled down for *in vitro* cultures efficiently oxygenate the tissue while protecting the cells from flow [24–26], but these systems have large dead volumes and are complex to manufacture and operate [25], thus motivating the present work.

The MePS approach here builds on an existing commercial multiwell-plate perfusion platform, the Liverchip[®], which has been used to model hepatic behaviors including drug–drug interaction [27], metastasis dormancy [28], hepatitis B infection [29], and non-alcoholic fatty liver disease (NAFLD) [30]. This platform was recently evaluated by the FDA for certain pre-clinical assays [31]. The commercial technology derives from a robust pneumatically-actuated microfluidic pumping technology [35] which enabled translation of the original design for a 3D perfused scaffold [36–39] from a format requiring an external peristaltic pump into a convenient and easy-to-seed multiwell plate format that minimized dead volumes and nearly eliminated depletion of lipophilic compounds from the circulating medium [6]. The scaffold in the original design comprised a thin ($\sim 250 \mu\text{m}$) silicon or polystyrene disk (PS) permeated by an array of hundreds of $\sim 300 \mu\text{m}$ diameter channels placed atop a microporous membrane, such that the membrane would hold isolated liver cells (hepatocytes or hepatocytes plus NPC) in place following initial seeding, then served to distribute flow relatively evenly to all channels in the scaffold after cells had attached to the scaffold and formed 3D tissue capturing some features of liver [6, 36–38]. This design, while easy to fabricate and use, exposes cells directly exposed to flow in ways that limiting the range of flow rates that the tissue can sustain, washes out poorly attached cells, and thus and restricts the total mass of tissue that the bioreactor can sustain. Given the recent interest in assays requiring more than a million cells [19, 40], we aimed to design a scaffold that could take advantage of the robust pumping power of the existing platform, but would support physiological function of larger cell masses.

Here, we report the design and fabrication of the first mesophysiological system or MePS for the long-term culture of PHH at mesoscale. The heart of the MePS is a scaffold design that leverages a custom high-resolution projection micro-stereolithography apparatus (PuSLA) [41, 42] to achieve a micro-to-meso geometry that is easy to seed, fosters 3D tissue formation/maintenance, and facilitates an unusual combination of diffusive and convective mass transfers to support oxygen, drug, and nutrient/metabolic product distribution throughout the tissue. The scaffold geometry, a lattice of hexagonal membrane-like units that guide flow through 3D porous microchannels from the periphery to a central draining channel, was designed and dimensionally scaled around the primary constraints of oxygen tension and tissue shear stress values, recognizing constraints that we and others have previously featured in simulations [6, 36, 43–47]. The built-in vasculature-like channels of the MePS scaffold feature nano and micro-holes in order to enhance permeability between the tissue and the media flow, capturing some aspects of the design of the AngioChip [48], but in a more intricate architecture facilitated by the PuSLA fabrication.

Although soft hydrogel structures have previously been produced by PuSLA [49–51], the mechanical and biocompatibility requirements for this application required development of new resin chemistry that allowed fast fabrication of a nanoporous material. This new material enables the fabrication of free-standing structures with intermediary softness between hydrogel formulations and hard plastics commercially used in 3D printing while not undergoing typical swelling that occurs with soft hydrogels. Further, all printing and post-printing processes can be performed in solution at room temperature, greatly facilitating the technical implementation of this method and its reproducibility.

Finally, recognizing that *in vitro* liver models are desirable for a range of applications from assessing metabolism and toxicity to disease modeling [27, 30, 52–56], we used a variety of metrics to assess the functional performance of PHH cultured in the MePS compared to the standard scaffold over a culture period of 3 weeks. Metrics include both standard functional metabolic assays (albumin and urea production and CYP450 activity) as well as a demonstration of disease modeling after characterizing the enabled lower inflammation profile in our MePS (through cytokine secretion) compared to standard scaffold. For the latter, motivated by the billions of individuals worldwide affected by non-alcoholic fatty liver disease [57] and type 2 diabetes [18, 58], we report here as a proof-of-concept the use of the MePS to replicate certain clinical features of a phenomenon common to both of these diseases, hepatic insulin resistance.

2. Materials and methods

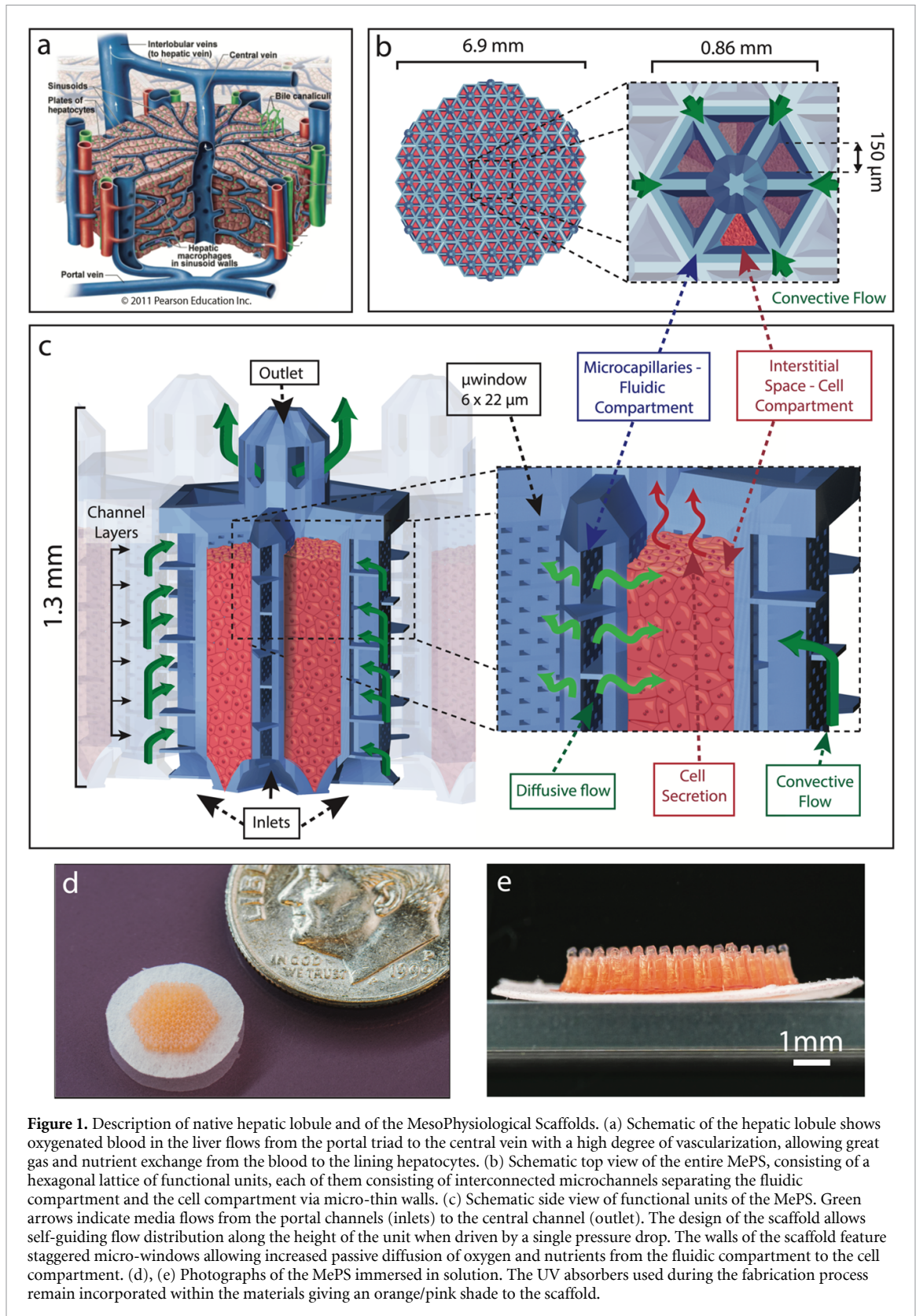
2.1. Design of the liver MesoPhysiological system

We designed a bioinspired scaffold (MePS) mimicking the native organization of the liver consisting of hepatic lobules (figure 1(a)) in which blood flows from hepatic arterioles and portal venules to central venules through liver sinusoids [59]. A schematic of the hepatic lobule and MePS can be found in figures 1 and S1 (available online at stacks.iop.org/BF/13/045024/mmedia). The entire scaffold consists of 61 functional units (figure 1(b)) in a hexagonal lattice made of photopolymerizable material, printed on a porous membrane.

The MePS is a mesoscale 3D microfluidic system made of a continuous network of microcapillaries guiding flow through its multiple layers of microchannels. The scaffold divides the space into two topologically distinct compartments (figures 1(b)–(c)). The first compartment, the interior of the microchannels, allows rapid convective flow through its conduits. It was designed to operate with a single pressure drop across the scaffold, and the geometry was optimized to generate a homogeneous self-guiding flow through the six parallel layers, each 120 μm tall and 60 μm wide. The second compartment outside of the microchannels creates the interstitial space in which the cells reside. Each functional unit hosts six triangular volumes in which hepatocytes form tissue and are shielded from damaging shear forces by the walls of the microchannels.

In order to sustain the high metabolic activity in the tissue, and generate modest interstitial flow, the two compartments are connected by micro windows (figure 1(c)) on the scaffold surfaces to increase nutrients and oxygen delivery from the fluidic compartment through passive diffusive flux and marginal convective flow across the micro-windows, which occupy 23% of MePS surface. Each functional unit is 750 \times 866 μm in size and 1.3 mm tall. The entire construct is 6.9 mm wide and can be easily scaled up to accommodate more tissue mass. The design of the functional unit is a scaled-down version of the hepatic lobule (1.2–2.4 mm in diameter) in order to account for the lack of oxygen-carrying heme, which inherently limits the length of oxygen diffusion in *in vitro* systems.

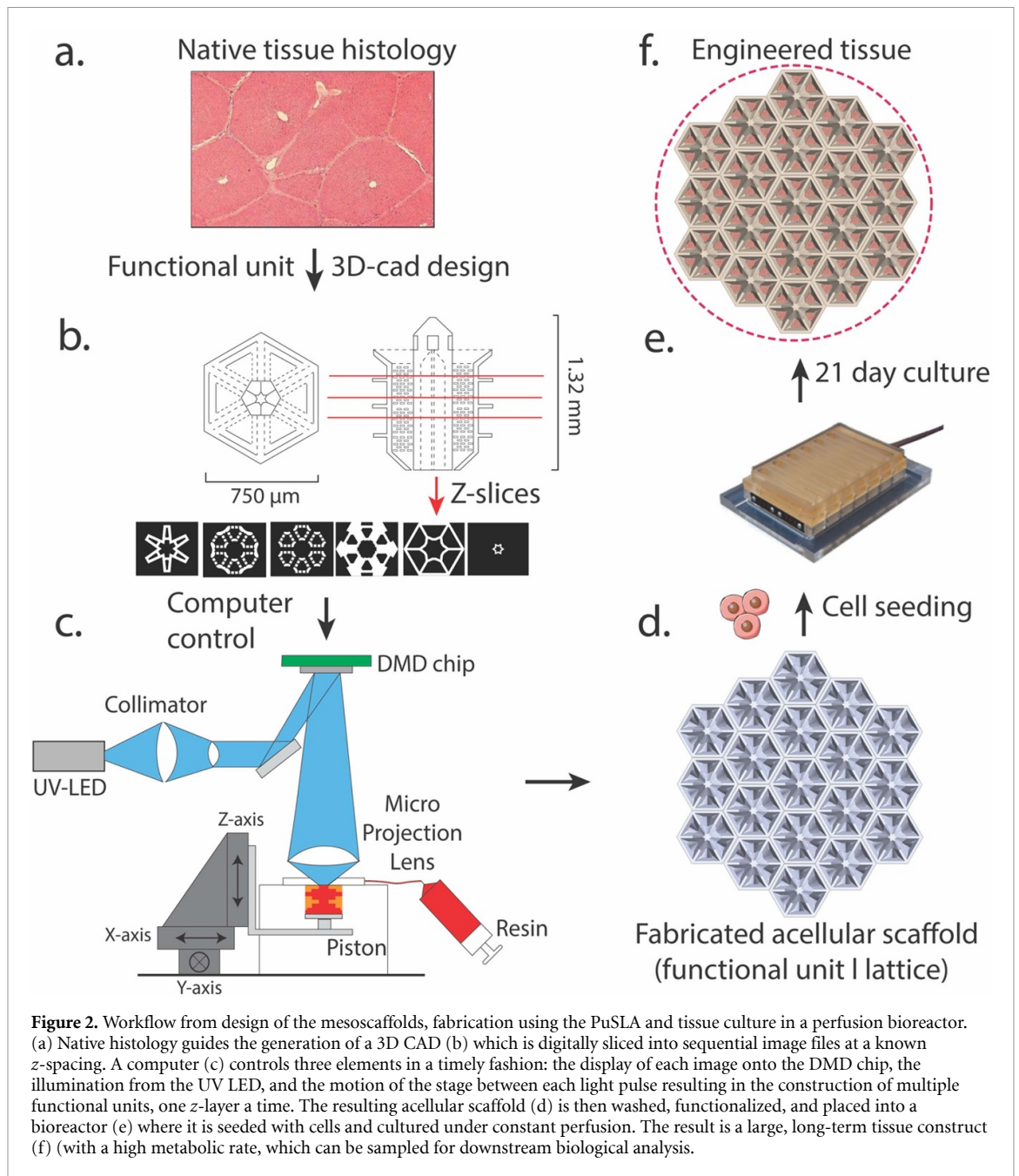
All 61 functional units making up the MePS are fluidically interconnected through a network of vertical channels (figure S1). Locally, fluid at each inlet (six per lobule) flows through a vertical channel that is shared between adjacent lobules and guides the flow through the parallel horizontal channels. These guiding interconnecting vertical channels reduce the hydraulic resistance of the entirety of the MePS due to geometric effect by guiding flow into larger channels, compared to design iterations of disjointed functional units (data not shown).



2.2. Fabrication of the MePS and implementation

Since the recent creation of the projection-micro-stereolithography apparatus (or P μ SLA) [41], a particular method of solid free-form (SFF) fabrication that relies on layer-by-layer photopolymerization, multiple studies have demonstrated its

ability to fabricate centimeter-scale 3D structures displaying micrometric features including with soft [51] and multi-material constructs [60], opening the door to a new realm of applications in tissue engineering. Given the great promises of this technology, we built a custom made P μ SLA with resolution



and throughput tailored for the SFF fabrication of the MePS (see supplementary data for information about the P μ SLA). The schematic of the fabrication and implementation of the MePS can be found in figure 2. We generated CAD files using Solidworks[®] 2018 of the bioinspired MePS (figure 2(a)), which were then sliced every 10 μm in the z-axis and converted into grayscale images. These images were then displayed by the P μ SLA (figure 2(b)) to fabricate the MePS on top of a 1 cm wide, 200 μm thick Durapore[®] porous membrane, which served as a substrate for the constructs (figure 2(c)). The z-step of the P μ SLA was set to 10 μm and a curing time adjusted to cure layers 14 μm thick. The outskirts of the 3D scaffolds was sealed by overcuring a contiguous layer of material. The resulting scaffolds were then processed to be

assembled within a bioreactor and seeded with cells to be cultured for 21 days (figures 2(d) and (e)).

2.3. Photopolymerizable resin

We designed a specialized formulation of the polymerizable resin that allowed fast fabrication of a relatively strong material allowing routine manual handling with high resolution, only requiring low-cost reagents easily available and allowing all steps to be performed at room temperature. Three monomers were tested (not shown) to optimize for material elasticity, mechanical resilience and swelling properties. The final resin was made by mixing six components (table 1) under a vented hood in the dark and stirred overnight until it resulted in a

Table 1. Chemical formulation of the photopolymerizable resin for the fabrication of the MePS using the P μ SLA.

Chemical	Function	Weight %
HDDA	Monomer	53.5
TMPE	Oligomer	19.9
Sudan I	UV absorber	0.20
Sudan IV	UV absorber	0.20
Irgacure [®] 819	Photoinitiator	1.50
PEG 200	Porogen	24.5

HDDA: 1,6 hexanediol dimethacrylate.

PEG 200: polyethylene glycole 200 MW.

TMPE: trimethylolpropane ethoxylatetriacrylate.

homogenous liquid that was stored in a PEEK light-blocking bottle.

2.4. Post-fabrication processes: material hydrophilization and preparation for cell culture

The SFF-fabricated meso-scaffolds were washed three times in ethanol and sterilized in a solution of 70% ethanol and handled with autoclaved microtweezers. The meso-scaffolds were then hydrophilized at room temperature in a six well plate overnight in a sterile-filtered solution of ethanol and deionized water (1:1 volume ratio) containing L-cystine hydrochloride and tris(2-carboxyethyl) phosphine hydrochloride (56 g L⁻¹ and 14 g L⁻¹ respectively), at a pH adjusted to 13.5 using sodium hydroxide. The meso-scaffolds were then washed five times in sterile deionized water on a rocking plate in a six well plate. The meso-scaffolds used for cell culture were then coated in a solution of rat tail collagen I diluted to 100 μ g ml⁻¹ in deionized water overnight at 4 °C. The meso-scaffolds were rapidly washed in PBS prior to insertion into the bioreactor.

2.5. Material characterization

The evaluation of the photopolymerizable material consisted of four aspects: (a) the kinetics of photopolymerization; (b) the elastic modulus of the material; (c) the coefficient of diffusion of oxygen; and (d) the adsorption properties of certain proteins and biochemicals.

All procedures and methods for characterization of these materials properties can be found in supplementary methods.

2.6. Simulations of fluid dynamics and oxygen in mesoscaffolds

To optimize the scaffold geometry and operation flow rate, we used COMSOL Multiphysics finite-element simulation software (COMSOL Inc., Burlington, MA, USA) to simulate the flow and oxygen transport in the MePS. A single functional unit of the entire meso-scaffold was imported into the COMSOL environment and external boundaries were

set as symmetry planes. The mesh for the finite-elements was created by the physics-controlled module and set as ‘fine’. In order to ensure physiological ranges of shear stress and oxygen, we performed two extreme case simulations corresponding to ‘worst-case-scenarios’. First, we assumed that the cell compartment offered zero hydraulic resistance to flow therefore providing an upper bound of interstitial flow and shear forces. Second, we modeled the cellular compartment as an impermeable volume, therefore preventing interstitial flow and limiting oxygen delivery to the tissue’s core. As a result, predictions from a solid cell compartment offered a lower bound of real oxygen tension within the tissue. All simulations were the result of steady-state derivations.

We selected Newtonian incompressible laminar flow and performed a parametric sweep at increasing flow rates from 1 to 5 μ l s⁻¹ at the inlet boundary. The no-slip boundary condition was set on the walls of the MePS. The pressure at the outlet of the MePS, 2 mm above the top of the meso-scaffold, was set to 0 Pa. Under these assumptions, the fluid dynamics is governed by the Navier–Stokes equation:

$$\rho \cdot u \nabla u = -\nabla p + \mu \nabla^2 u.$$

With u the fluid velocity, ρ and μ the respective density and viscosity of the medium. We computed the Reynolds numbers in the MePS defined as $Re = \frac{\rho u D_H}{\mu}$ with D the local hydraulic diameter of the flow.

We simulated oxygen levels in the MePS taking into account convection through the fluidic compartment, diffusion through the walls of the microcapillaries and consumption by the cells. The consumption rate R of the tissue was modeled using the Michaelis–Menten kinetic with v_{max} determined experimentally from O₂ measurements (see supplementary data). Given the model assumptions, the resulting governing equations were:

$$\begin{aligned} \partial c \partial t = 0 &= D_i \nabla^2 c - \nabla \cdot (u \cdot c) + R \\ R &= \frac{v_{max} \cdot c}{c + K_M} \end{aligned}$$

With c the concentration of O₂, D_i the coefficient of oxygen diffusion through the various materials (media, walls of the scaffold and tissue). The oxygen tension at the inlet of the scaffold was set at the constant saturation concentration (183 μ M, \sim 20 kPa), and the outlet was set as a free boundary of homogeneous oxygen distribution (2 mm above the scaffold). We computed Péclet Number and Damkohler number to compare convection, diffusion, and reaction rates using:

$$Pe = \frac{u_{ch} \cdot \delta_{eff}}{D_{eff}} = \frac{\text{convection}}{\text{diffusion}}$$

$$Da = \frac{v_{\max} \times \delta_t^2}{D_t \times c_{\text{wind}}} = \frac{\text{consumption}}{\text{diffusion}}.$$

With u_{ch} the velocity inside the channels, δ_{eff} and D_{eff} the effective length of diffusion and coefficient of diffusion respectively, δ_t the diameter of the tissue in each lobule, D_t the diffusion coefficient of oxygen in the tissue and c_{wind} the oxygen concentration at the exit of the windows.

2.7. Hepatocyte culture in bioreactor

Cryopreserved PHH from two donors (Hu8179 and AQL) were purchased from different vendors (ThermoFischer and BioIVT, respectively, both USA). Cells were thawed according to instructions provided by the vendors. Viability was assessed using the trypan blue exclusion test and was >93% for all lots. Cells were seeded into the Liverchip® (CN Bio Innovations, United Kingdom) which was placed into a humidified incubator at 37 °C at 5% CO₂. The Liverchip® houses 12 individual wells that are perfused continuously via recirculation of the media in a closed-loop fashion. Meso-scaffolds and polystyrene scaffolds (PS) were punched down into the bioreactor and sealed with compressing O-rings.

Cells were seeded in the PS scaffolds according to the instructions provided by the supplier (CN Bio Innovations). In brief, cells were seeded as a cell suspension with flow in the downward direction through the PS scaffold for 8 h at 1 $\mu\text{l s}^{-1}$ to allow tissue formation. The flow was thereafter inverted to upward direction until the end of the experiment. PHH were seeded at a density of 600 000 cells per scaffold in 1.4 ml of medium per well.

The protocol for seeding the cells into the MePS was optimized and adapted from the PS scaffold after testing out various technical parameters, which can be found in supplementary data. As a result of this optimization, for seeding of the MePS, the bioreactor was first left to equilibrate at 4 °C. Cells were seeded (day 0) as a cell suspension at a density of 1 $\times 10^6$ cells per scaffold by centrifuging the bioreactor at 100 g at 4 °C twice for 8 min. Media levels were adjusted in each well between the two centrifugation steps to achieve a total volume of 1.4 ml per well. Flow rate was set at 2.3 $\mu\text{l s}^{-1}$ in the downward direction for the first 24 h to allow microtissue formation and thereafter inverted to upward flow starting from day 1. Flowrate was increase to 2.7 $\mu\text{l s}^{-1}$ at day 5 and to 3.2 $\mu\text{l s}^{-1}$ at day 7 until the end of the experiment to sustain increasing oxygen consumption rate (OCR). Different flow patterns and flow rates were tested and results can be found in supplementary methods. This method presented here was found to be optimal from among those investigated.

From day 0 to day 1, the cells were maintained in William's E medium (WEM) containing primary hepatocyte thawing and plating supplements. From day 1 forward, the cells were maintained in WEM with

standard supplements. Full media composition can be found in supplementary methods. Complete media change was performed in each well every 2 days starting from day 1 until the end of the experiment. At each media change, 1 ml of the recirculating media was stored frozen at –80 °C for downstream biological assays. For the insulin-resistance study, two custom WEM (seeding and maintenance) were used with physiological levels of insulin and glucose (supplementary methods).

2.8. Oxygen consumption measurements

A custom made lid was machined in polysulfone (All Dimensions Manufacturing Inc., USA), with 12 ports to connect oxygen probes, allowing direct O₂ measurement at the inlet and outlet of the Liverchip® as previously described by Domansky *et al* [6]. Details about O₂ sensor calibration and assembly with the bioreactor can be found in supplementary methods and figure S43. Henry's law was used in order to convert the oxygen partial pressure drops to oxygen concentration drops. The OCR resulted in: $\text{OCR} = \Delta P \times H \times \varphi$, with ΔP (kPa) the partial pressure drop across the scaffolds, $H = 42.75 \text{ mol m}^{-3} \text{ kPa}^{-1}$ Henry's law constant of oxygen at 37 °C and φ the flow rate ($\text{m}^3 \text{ s}^{-1}$).

2.9. DNA extraction and quantification

We used the quantity of double-stranded DNA (dsDNA) as a method to estimate cell numbers in the scaffolds as described in previous work [61]. PS scaffolds and MePS meso-scaffolds containing hepatic tissues were removed from the Liverchip® and flash-frozen in a lysis solution of 50 mM Tris, 10% glycerol, 150 mM NaCl and 1% NP-40. Similarly, cryopreserved PHH were thawed, resuspended at a concentration of 1 $\times 10^6$ cells ml^{-1} , and directly flash-frozen in the lysis buffer to serve as a reference point. All samples were thawed at 37 °C, triturated using a pestle homogenizer, and sonicated for 5 min. DNA was purified using QIAamp DNA Mini Kit (Qiagen) according to the manufacturer protocol. Samples were then diluted in order to fit the linear range of the standard curve and quantified using Quanti-iT™ Picogreen® dsDNA assay kit according to the manufacturer's instruction. Samples from the cell-counted cryopreserved PHH vials were serially diluted in order to count obtain the reference DNA content per viable cell.

2.10. Determining LDH and ALT concentration

Lactate dehydrogenase (LDH) release as a cytotoxic marker and alanine aminotransferase (ALT) as a specific liver damage marker were measured using enzymatic colorimetric kits (from Promega and Abcam, respectively). Samples were thawed to room temperature and prepared according to the suppliers' instructions. In brief, for LDH release, samples were mixed with the substrate reconstituted in assay

buffer into a 96 well plate at 37 °C, and the reaction was stopped at 30 min. For ALT release, samples were diluted in duplicates to fit the standard curve and prepared according to the manufacturer protocol. Optical density was measured using a SpectraMAX plate reader (Molecular Devices, USA) at the end of the reaction for LDH at 490 nm, and every 5 min at 570 nm for one hour for ALT to obtain the conversion rate.

2.11. Determining rates of albumin and urea synthesis

Albumin secretion and urea synthesis were measured by enzyme-linked immunosorbent assay (ELISA) kits. Samples were thawed to room temperature, prepared according to the supplier instructions, and pipetted into a high-binding 96 well plate. All samples and standards were diluted in duplicates in the supplied conjugated diluent buffer to fit the standard curve and prepared in duplicates. The remaining steps were performed at room temperature according to the manufacturer protocol, and absorbance was measured using a SpectraMAX plate reader at 450 nm and 570 nm, respectively.

2.12. Determining P450 enzymes activity

The phase I metabolic activity of the cytochrome P450 (CYP) enzymes of the isoforms CYP3A4 and CYP1A2 were measured using the P450-Glo™ kits (Promega) with Luciferin-IPA and Luciferin-1A2 respectively. The Luciferin substrates were diluted to 3 μ M and 6 μ M respectively, in two separate maintenance medias. The Luciferin-IPA was first incubated for 1 h under perfusion in the Liverchip® followed by two full media changes, followed by the Luciferin-1A2 incubated for 3 h. Collected samples were added to a white-walled 96 well plate with a standard prepared using a serial dilution of click beetle luciferin potassium salt. Luminescence was measured in duplicate wells using a SpectraMAX plate reader.

2.13. Measurements of cytokine production

Cell supernatants were analyzed using a custom Luminex panel from R&D systems. Samples were processed according to the manufacturer's instructions adapted to a 384-well plate. Briefly, samples were diluted by 2 and 50-fold in technical duplicates on the plate. Samples were mixed with magnetic capture beads overnight, followed by plate washing, addition of detection beads, washing, Streptavidin-PE, and final washing. Plates were run on the FLEXMAP 3D (BioRad) with parameters specified by the panel kit manufacturer. Raw MFI values were fitted to standard curves using five-point logistic regression with xPONENT software (Luminex Corp). Downstream data analysis exported from xPONENT was performed using MATLAB 2020a with Bioinformatics Toolbox (MathWorks) (see supplementary data for detail of the analysis).

2.14. Imaging

For direct imaging inside the Liverchip®, the bioreactor was momentarily detached from the perfusion system and quickly imaged under a stereoscope (STereo Discovery.V12, Zeiss). For immunohistochemistry, the scaffolds were removed from the bioreactor and washed with PBS. The samples were fixed in 4% paraformaldehyde in the Liverchip® under a biosafety cabinet under perfusion for 30 min at room temperature. The samples were permeabilized after fixation with 0.1% Triton™ X-100 in PBS (Sigma Aldrich, USA), and stained on a rocking plate in a cold room at 4 °C overnight with a 1:200 dilution of Alexa488 Phalloidin and counterstained with DAPI diluted 1:5000 in PBS.

For SEM imaging, samples were washed in ethanol and immersed in hexamethyldisilazane. The samples were left to air dry under a fume hood and sputter-coated in gold.

For LIVE/DEAD imaging, a live/dead kit (molecular probes) was used. The fluorescent probes were diluted according to the manufacturer's protocol in maintenance media and circulated for 1 h within the Liverchip®. Scaffolds were thereafter removed from the Liverchip, rinsed in PBS and immediately imaged in a fluorescent microscope (BZ-X710, Keyence).

2.15. Determining insulin clearance and gluconeogenesis

For the hyperinsulinemia and hyperglycemia study, each well of the bioreactor was fed with a total volume of 1.6 ml of medium. 100 μ l of recirculating media was collected at 8, 24 and 48 h after each media change and frozen at -80 °C. Insulin clearance was measured using an ELISA kit following the supplier instructions. To measure gluconeogenesis in the MePS, the cells were first starved in medium with no insulin nor glucose for 1 h and thereafter conditioned for 24 h at day 15 in a glucose-free WEM based medium with a titer of insulin (0, 0.1 and 10 nM). The conditioned media was then collected, and glucose production was measured using a colorimetric assay (Abcam). More details on this model can be found elsewhere [62].

3. Results

We set out to leverage the advantages of PuSLA to manufacture an MePS providing physiological levels of oxygen and shear stress to a meso-scale liver tissue mass (i.e. >10⁶ cells in a compact 3D format). We also investigated canonical markers of hepatic function *in vitro* and demonstrated features of an insulin-resistance phenotype.

3.1. Projection μ -StereoLithography apparatus and material properties

Most fabrication techniques for microfluidic devices are often complicated and time-consuming, requiring

costly equipment in sophisticated cleanroom facilities [63]. Furthermore, their 2.5D fabrication process limits, by nature, the range of 3D designs that can be manufactured. Finally, these methods are usually difficult to scale up when considering the need to integrate the microfluidics within a perfusion system, therefore limiting the size of the tissue. As a result, various SFF methods are appealing alternatives to fabricate microperfused devices, reducing both the cost and complexity of fabrication. Here we present a fabrication technique which rivals traditional SU8 lithography in terms of resolution but allows rapid fabrication of true 3D constructs with high aspect ratio at centimetric scale. The photopolymerization process (figure 3(a)) enables the creation of a nanoporous material (figures 3(b) and (c)). SEM images of an intermediate design of our mesoscaffold constructs can be seen in figures 3(d)–(g). This design does not contain interconnected lobules, and is used here to illustrate feature resolution, which is easier to visualize in this design. The P μ SLA enables the fabrication of a lattice of functional units (figure (d)) consisting of capillary channels with thin walls (44 μ m) and open windows (6–22 μ m wide, figure 3(f)), allowing precise control over the construct geometry. Owing to the additive nature of the fabrication process, the P μ SLA was capable of fabricating structures with high aspect ratio (figure 3(g)) while conserving resolution of the fabrication technique. Full characterization of the fabrication resolution is seen in figure S5. While both diffraction of the light and uneven illumination limited precision of the technique, $6.3 \times 22.7 \mu$ m windows were reliably manufactured (figure S5) with a resolution of $2.3 \times 6.8 \mu$ m across the entire MePS (6.9 wide \times 1.3 mm tall) within only 187 min. The inherent tradeoff between resolution and throughput guided the design of the MePS so that flow distribution remained unaffected by small defects of fabrication (see figure S12), allowing less stringent criteria for rapid fabrication of the scaffolds.

The resin was a key component of the SLA fabrication technique, and its chemical design was motivated by three criteria: the speed of polymerization, the mechanical properties of the resulting material, and its degree of porosity. Small variations in UV absorber (from 0.1 to 0.25 w%) had a dramatic effect on the kinetics of photopolymerization (figure S6), with a smaller effect from the photoinitiator concentrations. We chose a concentration of UV absorber and photoinitiator (0.2 w% and 1.5 w%, respectively) that maximized E_c and minimized D_p in order to increase the Z resolution of the photopolymerization process while maximizing throughput.

PHH functions are negatively affected by substrate mechanical properties, characterized in part by the Young's modulus, E [64]. We therefore targeted a resin chemistry that resulted in a much softer bulk modulus ($E = 310 \pm 6.8$ kPa) than

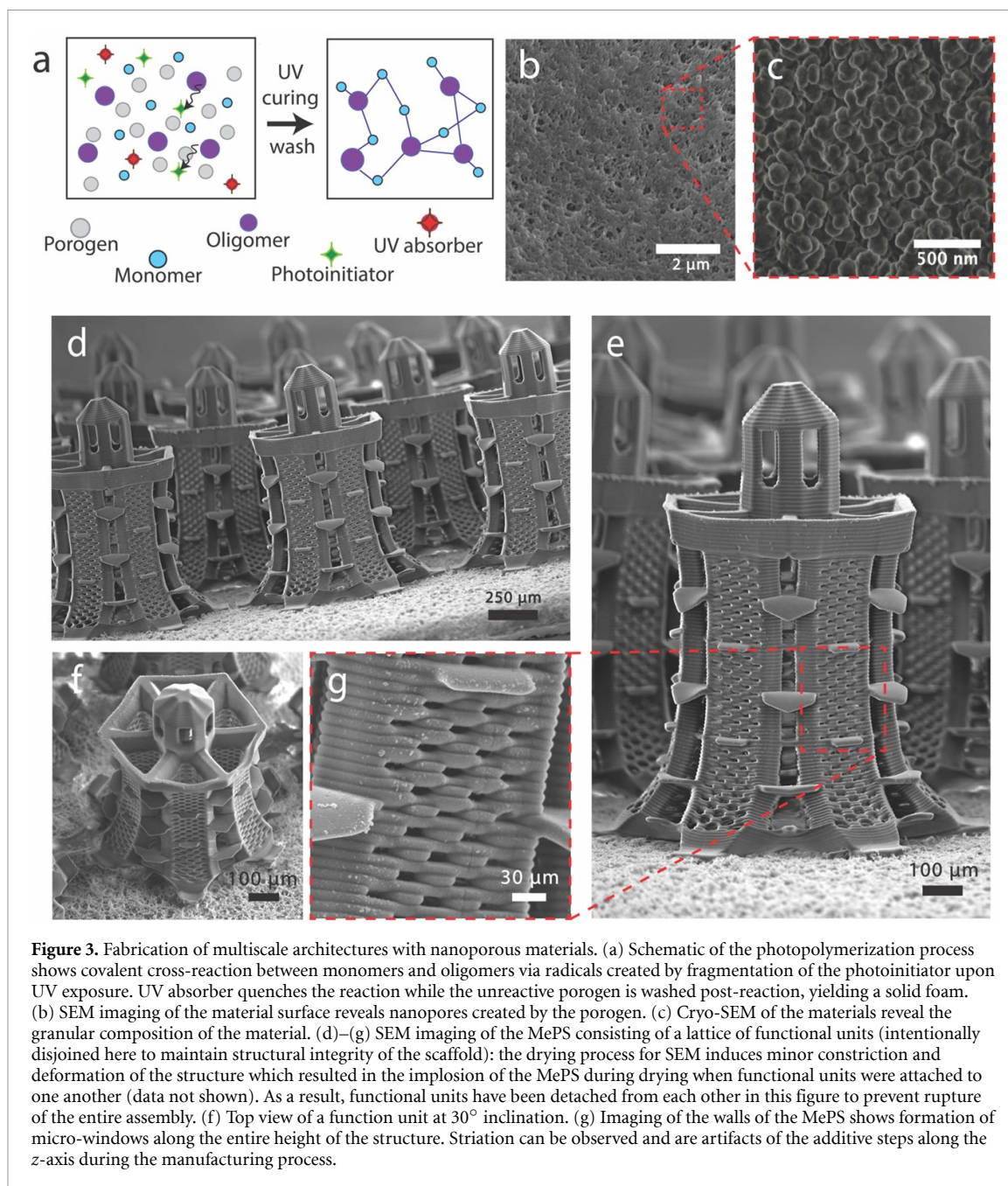
Table 2. Fabrication resolution, MePS features size, and material properties.

Property	Value
P μ SLA x, y resolution	6.8 μ m
P μ SLA z resolution	2.3 μ m
P μ SLA printing time (/scaffold)	182 min
MePS diameter	6.9 mm
MePS height	1.3 mm
Material 2D porosity	$16 \pm 1.1\%$
Pore size	142 ± 110 nm
Material D_{O_2} coefficient ($\times 10^{10}$)	3.1 ± 0.4 m ² s ⁻¹
Material Young's modulus	310 ± 6.8 kPa

polystyrene ($E = 2.91$ GPa [65]). While this E value is still greater than the native microenvironment of liver, the nanoporosity may contribute to mechanical signal transduction in favorable ways [66, 67]. Indeed, numerous studies have established the favorable effect of nanopores on stiff substrate with respect to mechanotransduction in epithelial cells [68, 69]; in addition, mucosal epithelial cells from lung, intestine, endometrium, and other tissues cultured on stiff but porous Transwell membranes retain physiological function without evidence of fibrotic response. The resulting material was strong enough to allow manual handling of the SFF-produced meso-scaffolds in solution without damaging them.

Measurements of porosity (figure 3(b)) revealed the creation of dense nanopores (142 nm \pm 110 nm) at 16% 2D porosity from the spinodal decomposition of the porogen during the fabrication process. The addition of nanopores resulted in an elevated coefficient of diffusion of oxygen $D_{O_2} = 3.1 \pm 0.4 \times 10^{-10}$ m² s⁻¹ (supplementary methods), 26-fold greater than regular plastics such as polystyrene ($D_{O_2}^{[Polystyrene]} = 0.12 \times 10^{-10}$ m² s⁻¹ [70]), allowing increased flux between the fluidic and cellular compartments.

SLA generally requires post-processing [71] with a drying step and a light exposure step to quench unreacted groups on the surface. Given the size of the features on the MePS, direct drying of the scaffolds resulted in mechanical failure of the structure by surface tension. Instead, we developed a process to functionalize the material using L-cystine, a zwitterionic amino acid, that increased both the hydrophilicity and biocompatibility of the material. With this workflow, the MePS remained constantly immersed in solution throughout its entire lifetime, therefore eliminating the risk of fracture and bubble formations. The effects of the functionalization on scaffold response to deformation in solution are shown pictorially in figure S7. Derivation of the oxygen diffusion coefficient in the nanoporous scaffold wall (reported in table 2) was performed using data in figure S8. The final meso-scaffolds exhibited



minimal adsorption of proteins across a wide range of protein sizes and properties (insulin, albumin, TNF- α , TGF α , and EGF; figure S8).

3.2. Computational simulations of flow and oxygenation

The geometry of the MePS was optimized to maximize the volume of the cellular compartment while maintaining physiological levels of oxygen and shear forces. Results from the simulations can be found in figure 4. We calculated the Reynolds numbers and found a maximal value $Re = 0.21$ at the outlet of the scaffolds within the central channel where velocity peaked at 1.68 mm (at flow rate $\varphi = 3.2 \mu\text{l s}^{-1}$) (figure 4(a)), computationally validating the laminar

nature of the flow. Flow in the MePS through each of the six layers of the microchannels ranged from 14.2% to 19.8% of the total flow, suggesting a homogenous flow distribution along with the height of the MePS. Predicted shear forces experienced by the tissue ranged up to 2 mPa, increasing along with the height of the MePS (figure 4(a)) with a median value at 0.9 mPa, far below the critical shear stress of 1.6 mPa experienced by the hepatocytes in the PS scaffolds. Viscous stress increased linearly with flow rate (figure 4(b)) and presented an uneven distribution throughout the MePS, limiting flow rates exceeding $3.7 \mu\text{l s}^{-1}$. Marginal interstitial flow was predicted (13.8% of total flow), implying that the windows were slightly permissive to flow through the cellular compartment.

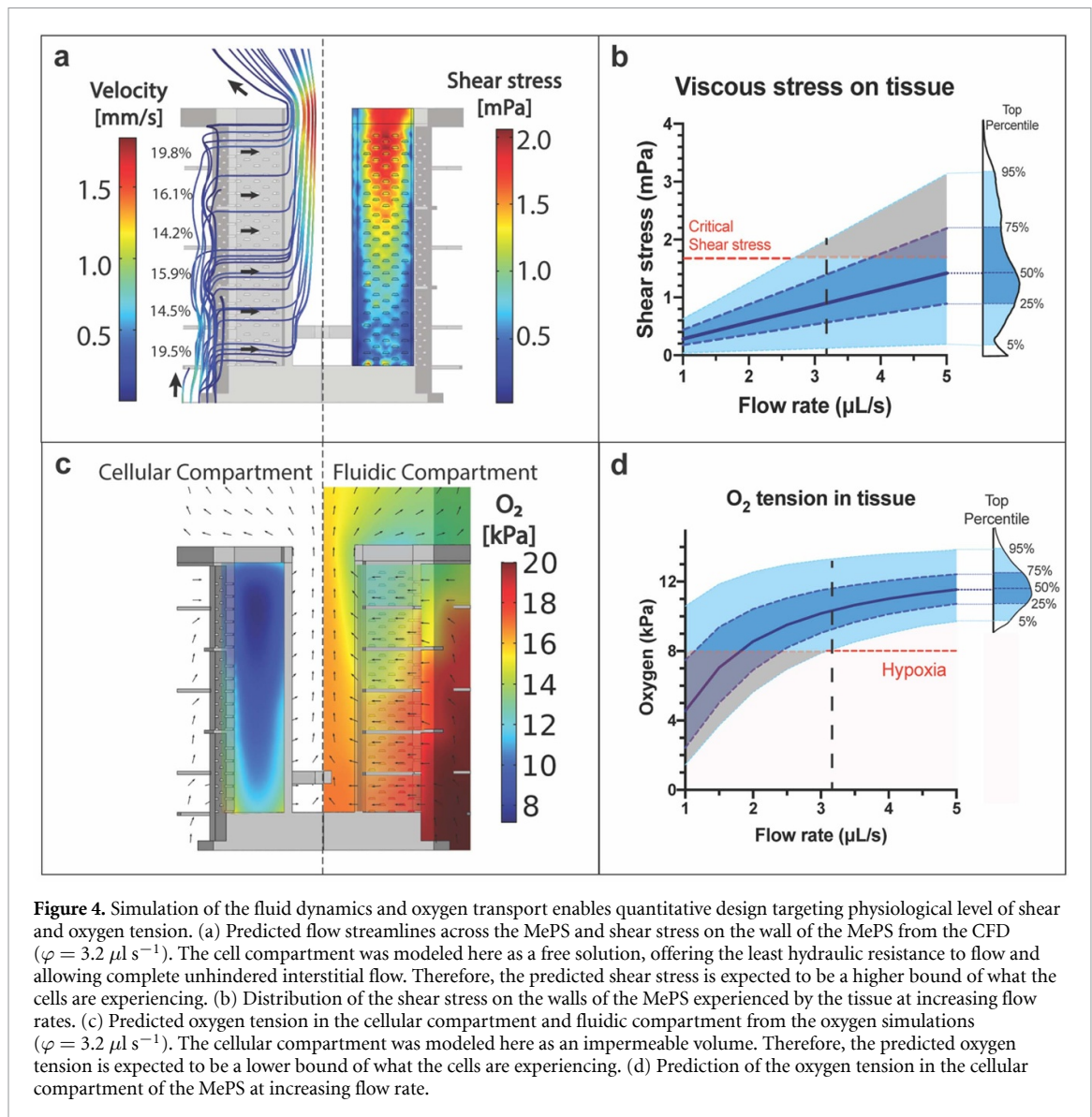


Figure 4. Simulation of the fluid dynamics and oxygen transport enables quantitative design targeting physiological level of shear and oxygen tension. (a) Predicted flow streamlines across the MePS and shear stress on the wall of the MePS from the CFD ($\varphi = 3.2 \mu\text{l s}^{-1}$). The cell compartment was modeled here as a free solution, offering the least hydraulic resistance to flow and allowing complete unhindered interstitial flow. Therefore, the predicted shear stress is expected to be a higher bound of what the cells are experiencing. (b) Distribution of the shear stress on the walls of the MePS experienced by the tissue at increasing flow rates. (c) Predicted oxygen tension in the cellular compartment and fluidic compartment from the oxygen simulations ($\varphi = 3.2 \mu\text{l s}^{-1}$). The cellular compartment was modeled here as an impermeable volume. Therefore, the predicted oxygen tension is expected to be a lower bound of what the cells are experiencing. (d) Prediction of the oxygen tension in the cellular compartment of the MePS at increasing flow rate.

Predicted oxygen levels in tissue (figure 4(c)) ranged from 7.9 to 13.3 kPa with a median value of 10.1 kPa, mirroring oxygen levels of the oxygenated regions of the hepatic lobule of 8.7 kPa [72]. Péclet number calculation gave $\text{Pé} = 214 \gg 1$ validating dominance of the convective flux over diffusive flux in the MePS. The calculation of the Damkhöler number gave $\text{Da} = 34$, which was found to be greater than other liver MPS operating in the 0.55–2 range [6] which can be explained in part by the microscopic scale of these other MPS. We also calculated the Damkhöler number of the MePS in the absence of windows giving $\text{Da} = 580$, indicating that the nanoporosity of the material alone was not enough to ensure sufficient oxygenation of the tissue. The numerical simulations validated the mode of operation of the MePS: its design allowed elevated convective flow through its network of microcapillaries while shielding the tissue from damaging shear forces. Careful design and fabrication of side windows permitted improved oxygen delivery

to the core of the tissue with minimal interstitial flow.

3.3. Seeding efficiency in MPS and MePS

Seeding of 1×10^6 hepatocytes into the MePS resulted in dense live tissue in the cellular compartment of the scaffold as seen from figure 5. Traditional MPSs usually require minuscule amounts of cells for their operation [4], but when assembled with their perfusion system, they generally result in devices with a large media-to-cell ratio far from physiological levels. Furthermore, protocols usually involve seeding an excess of biological material, which can bias downstream analysis when normalizing to number of cells seeded. In order to assess the number of remaining cells in the scaffolds, we measured the quantity of dsDNA in the MPS and our SFF-produced MePS after 7 days of culture. As seen in figure 6 a, when seeded at an increasing number of hepatocytes, both MPS and MePS presented a bell-like curve, indicating an optimal seeding density for their operations.

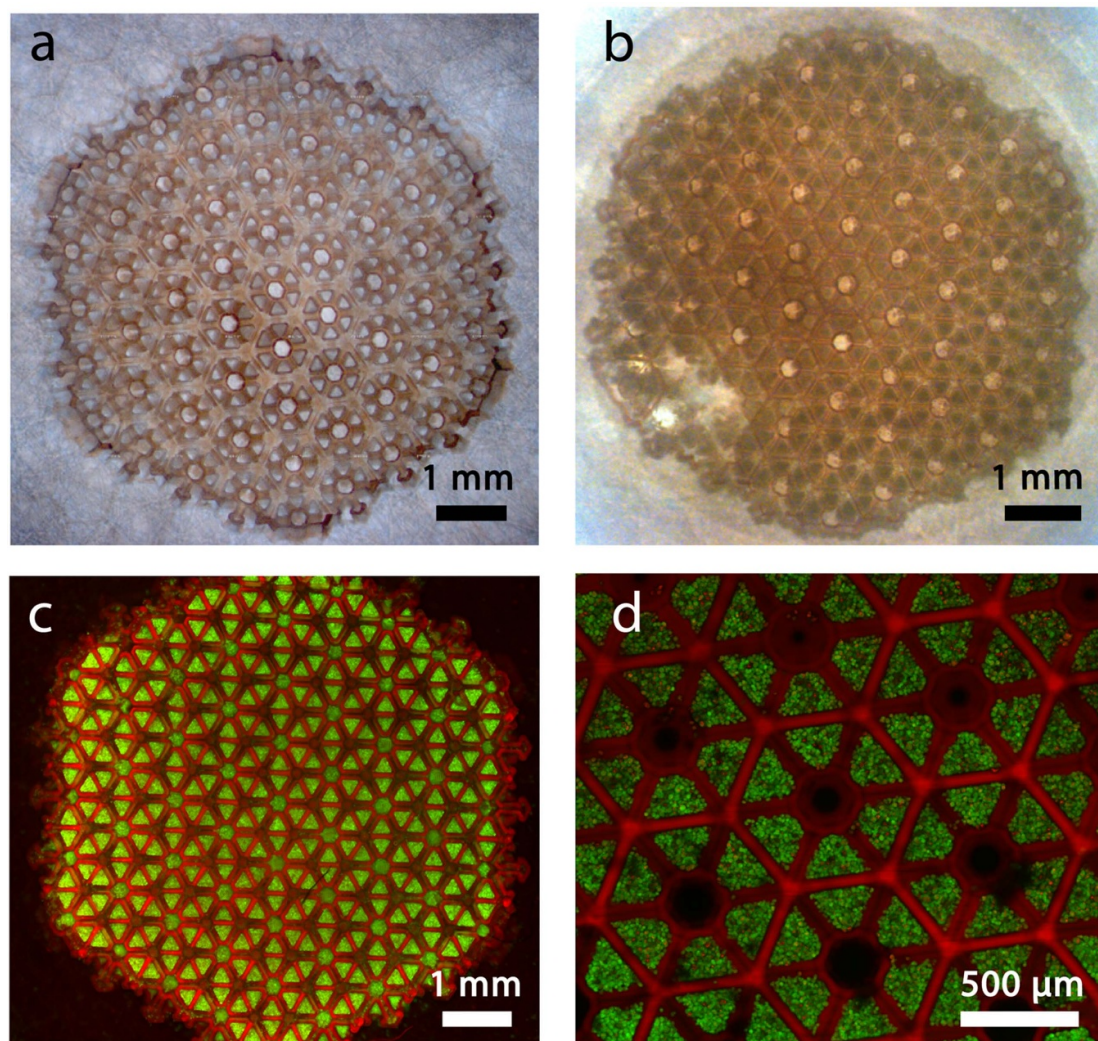


Figure 5. Imaging of hepatic culture within MePS. (a) Stereoscope images of empty mesoscaffold before seeding and after 15 days of culture after fixation (b). Darkened interstitial volumes within the scaffolds suggest dense, healthy tissue. Damaged area can be seen during the removal process within the Liverchip (arrow). (c), (d) Live/dead imaging of the MePS (green/red) after 5 days of culture. Imaging of the scaffold indicates live cells within the cellular compartment of the MePS. Dyes used during the fabrication process cause auto-fluorescence of the structure in the red channel. (d) Stacked z-projection from fluorescently labelled LIVE/DEAD hepatocytes reveals (D) cell morphology densely packed between scaffold channels.

For the PS scaffolds, the DNA content peaked at 6×10^5 cells per scaffold with a total dsDNA content of $3.2 \mu\text{g} \pm 0.3$, corresponding to 65% of the total number of cells at seeding. For our MePS, total DNA content maxed when seeded at 1×10^6 cells at $6.5 \pm 0.3 \mu\text{g}$ per scaffold, corresponding to 82% of the total number of cells seeded. These results suggested that our MePS could host a large mass of primary hepatocytes with minimal amount of media recirculating volume (1.4 ml).

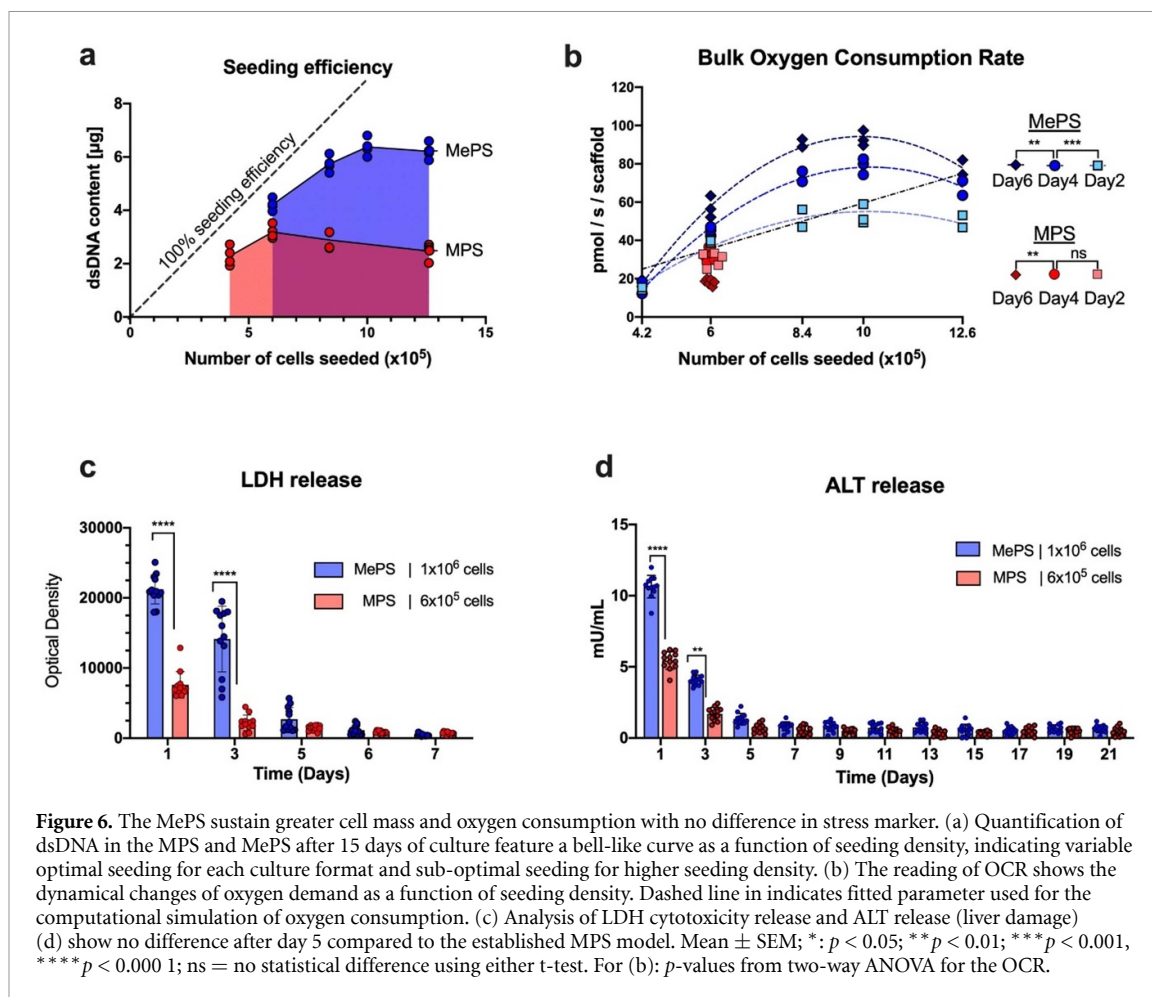
3.4. Elevated OCR in the MePS

Oxygen gradients in hepatic lobule affect hepatic function both in healthy and diseased states [72]. In order to monitor hepatic viability and function in our *in vitro* system, we measured the OCR (OCR, figure 6(b)) of the tissues cultured in the standard PS scaffold and MePS over the course of 7 days at an increasing number of cells. Raw data can be found

in supplementary data. The OCR in the PS scaffold gradually declined over the course of the experiment from 32 to 19 pmol s^{-1} at its optimal seeding density of 6×10^5 cells. Conversely, the OCR in the SFF-manufactured MePS gradually increased over the course of the experiment. When seeded at 1×10^6 cells, the OCR rose from 43 to 95 pmol s^{-1} from day 2 to day 6. The differential trajectory of OCR between the PS scaffold and MePS suggested that in addition to promoting better long-term health of hepatocytes, the tissue in the SFF-manufactured scaffold was increasing its function over the length of the culture.

3.5. LDH and ALT release

To assess viability of the cells in the MePS, levels of LDH and ALT were continuously sampled from the recirculating media to monitor cytotoxicity and potential liver damage. We used the commercial scaffold made of micromachined PS as a



benchmark comparison to our SFF-manufactured meso-scaffolds. Similarly to other physiological *in vitro* cultures of cryopreserved human hepatocytes [73–75], LDH and ALT secretion rates were elevated upon thawing for the first 3 days of adaption in both culture formats as cells adapted to culture conditions. Levels of LDH in the MePS dropped significantly after day 5 (figure 6(c)) and remained low to similar background values as the PS condition. Similarly, ALT release in the MePS (figure 6(d)) significantly dropped throughout the first 5 days of culture and remained low ($<0.8 \text{ mU ml}^{-1}$) for the remainder of the culture (21 days). These drops were concomitant with a rise in the rates of albumin production (see below). Given the previous characterization of the commercial PS system in the Liverchip ©[6], the overall low concentrations of LDH and ALT in the MePS support the conclusion that cells were viable, even when seeded with a greater number of hepatocytes (1×10^6 cells in the MePS versus 0.6×10^6 cells in the MPS).

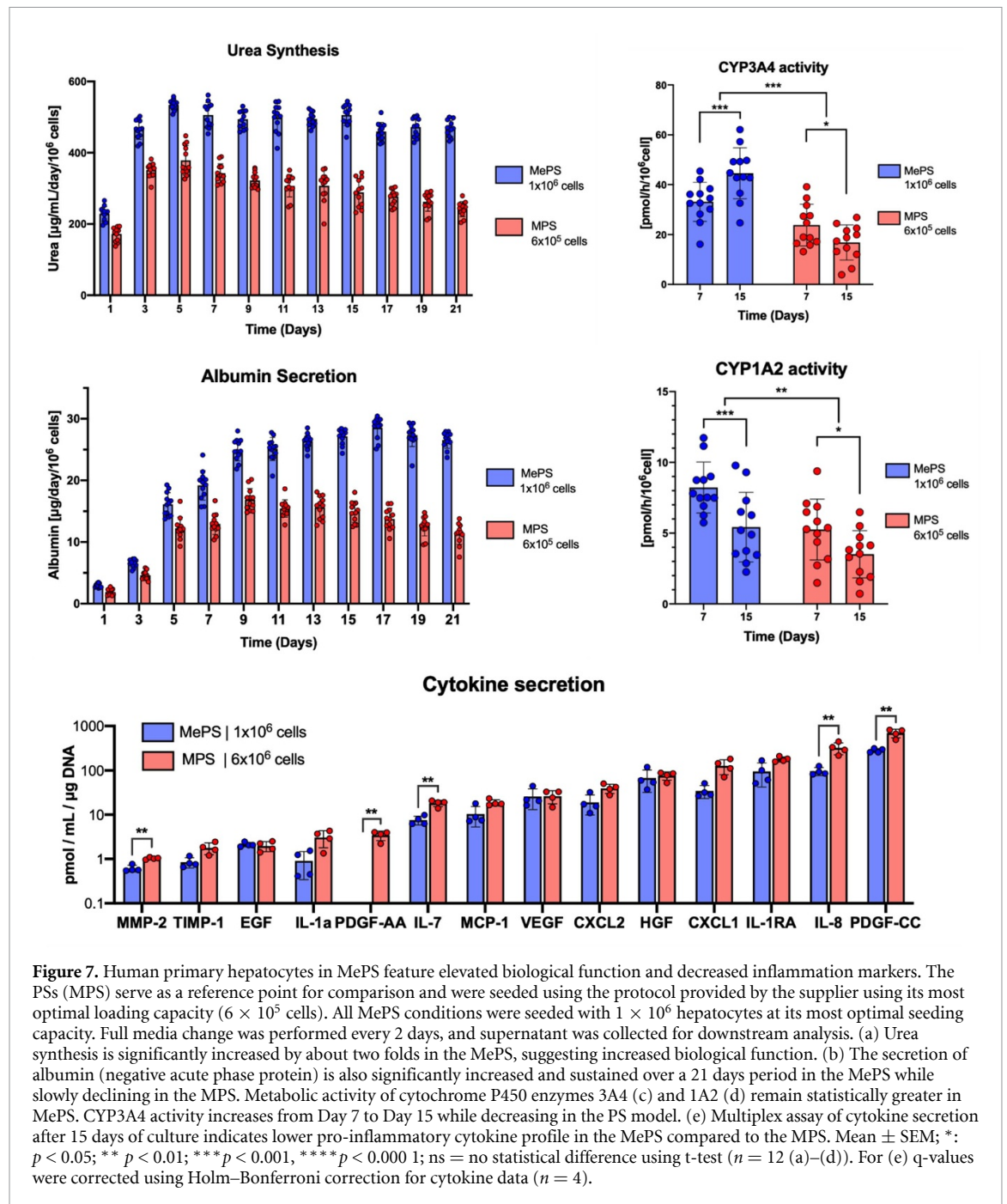
3.6. Albumin secretion and urea synthesis

We measured albumin levels and urea secretion as canonical indicators of hepatocyte function. The PS scaffolds served as a benchmark comparison to our MePS. Both conditions featured an increase of urea

synthesis (figure 7(a)) from the day of seeding to peak at day 5. Urea synthesis in the MePS remained stable until the end of the experiment (21 days total) at elevated levels ($>70 \mu\text{g ml d}^{-1} \mu\text{g DNA}$), much greater than the MPS ($<32 \mu\text{g ml d}^{-1} \mu\text{g DNA}$). Similarly, albumin secretion in both conditions increased drastically from day 0 up to day 7 (figure 7(b)). Albumin levels thereafter remained overall constant in the MePS ($\sim 5 \mu\text{g ml d}^{-1} \mu\text{g DNA}$) at values much higher than the PS condition, which started to decline after the 9th day of culture ($<3 \mu\text{g ml day}^{-1} \mu\text{g DNA}$). Given the importance of albumin [76] and urea synthesis [77] as benchmark biomarkers of hepatic function, these results support the conclusion that cells in the MePS exhibited elevated hepatic function compared to commercial scaffolds. The absolute values of urea and albumin synthesis also support the conclusion that a considerable number of cells participated in the function of the entire MePS. Furthermore, the stable levels of urea and albumin synthesis suggest that long-term culture of 21 days is possible. ($n = 6$ repeated twice for each donor with $n_{\text{donor}} = 2$).

3.7. Cytochrome P450 activities

We measured the activity of two prominent cytochrome P450 enzymes (CYP3A4 and CYP1A2,



figures 7(c) and (d) which account for 40% of xenobiotic activity [78] of the liver to assess the metabolic activity of the cells in the MePS. The PS scaffolds served as a benchmark comparison. CYP3A4 activity in the MePS increased from day 7 to day 15 while decreasing in the PS condition. Normalized CYP3A4 activity in the MePS showed enhanced conversation rate ($7.4 \text{ pmol h } \mu\text{g}^{-1} \text{ DNA}$ at day 15), much greater than in the PS condition ($2.7 \text{ pmol h } \mu\text{g}^{-1} \text{ DNA}$ at day 15). Similarly, cells in the MePS showed elevated CYP1A2 activity ($1.4 \text{ pmol h } \mu\text{g}^{-1} \text{ DNA}$ at day 7, figure 6(f)) compared to the PS condition ($0.83 \text{ pmol h } \mu\text{g}^{-1} \text{ DNA}$ at day 7). Both scaffolds featured a decrease of CYP1A2 activity from day 7 to day 15, which is expected as CYP1A2 is often elevated

in stress [79, 80]. Given the importance of CYP3A4 and CYP1A2 enzymes *in vivo*, these results showed that culturing hepatocytes in the MePS can improve metabolic activity for a long time.

3.8. Cytokine production

Systemic inflammatory crosstalk is important in many diseases [81] including those afflicting liver, hence basal inflammation profiles are useful in determining physiological conditions for *in vitro* disease models [82]. Thus, we measured secretion rates of multiple cytokines, chemokines and growth factors (C/C/GFs) in order to establish the inflammation profile of the cells in the MePS in comparison to the PS condition. Out of the 37 C/C/GF analyzed

(figure 6(e)) in the media, only 14 were at detectable levels after 48 h. From these 14 cytokines, 5 (MMP2, PDGF-AA, IL-7, IL-8, and PDGF-CC) were significantly decreased in the MePS compared to the PS condition and none were elevated when normalized for DNA content. We reiterate here that tests of representative C/C/GF for interaction with the meso-scaffold (figure S9) indicate that loss due to protein absorption to the scaffold is negligible. These results support the conclusion that the MePS enables a more physiological culture of hepatocytes compared to the commercial PS system, with a lower inflammation profile at basal levels.

3.9. Insulin-resistant model in hepatic mesophysiological MePS

Finally, we investigated as a proof of concept whether this new system could recapitulate features of hepatic insulin resistance, a clinical features of type 2 diabetes (T2D) and NAFLD [58, 83] as we describe in more detail elsewhere [62]. We tested the effect of long term culture media on primary hepatocytes in the MePS for 15 days: a physiological media (figures 8(a) and (b)) with glucose and insulin levels similar to portal levels *in vivo* (5.5 mM and 200 pM respectively [84, 85]), and an hyperinsulinemic and hyperglycemic media (thereafter referred as T2D media) in which levels of insulin and glucose were intended to mirror postprandial values of patients exhibiting hyper insulin secretion (11 mM and 1000 pM respectively). Full composition of both media can be found in supplementary data.

We measured the rate of insulin cleared from the media in the two conditions (figure 8(c)) across multiple timepoints. The insulin clearance remained constant throughout the experiment in the physiological media, with a total clearance rate after 48 h of culture around 75%. On the contrary, the hepatocytes in the T2D media started losing the ability to clear insulin starting from day 9, steadily declining from 76% at day 5 down to 49% at day 15; this finding is consistent with data from additional donors cultured in the standard MPS as reported elsewhere [62]. We also tested for CYP450 activity, as clinical data have reported a reduction of CYP3A4 and CYP1A2 activity in diabetic patients. We found that the activity of both enzymes (figures 8(d) and (e) in both media were at comparable levels at day 7, but the activity of both CYPs in the T2D media was dramatically reduced compared to the physiological media at day 15. CYP3A4 activity was reduced by 2–3 folds in the T2D media and by 48% for the CYP1A2.

A critical function of the liver regarding T2D is its ability to both store and release glucose *de novo* (gluconeogenesis) when exposed to low levels of insulin in the serum (<0.1 nM) [58]. This function is altered in diabetic patients when the liver is excessively exposed

to a high amount of insulin. We measured gluconeogenesis capacity of PHH when exposed to increasing concentrations of insulin (0, 0.1 and 10 nM) after being conditioned in the two different media (figure 8(f)). Glucose production of the cells maintained in physiological media behaved as expected from healthy *in vivo* data: the cells secreted 160 μ M of glucose in the absence of insulin, and the secretion was totally inhibited at the highest concentration of insulin. In stark contrast, the cells maintained in T2D media produced a greater amount of glucose, close to 400 μ M in the absence of insulin, and this secretion could not be inhibited by a high level of insulin (10 nM) with a resulting glucose output of 180 μ M.

These three features together (the decline of insulin clearance, the diminished CYP activities, and the overproduction of glucose even at an elevated level of insulin) suggest that the hepatocytes in the MePS have established an insulin resistant-like phenotype recapitulating some clinical features observed in T2D. The gradual decline over time of the insulin clearance and the difference of CYP activity between day 7 and 15 seem to indicate that this phenotype required long term exposure to hyperinsulinemic and hyperglycemic levels for the phenotype to progress.

4. Discussion

The results obtained in this study demonstrate that PuSLA printing can be used to fabricate mesoscale scaffolds with microscale 3D fluidic networks, allowing sustained 3D primary liver cultures. One of the driving motivations for this work was the need to create a mesoscale system to bridge the gap between *in vitro* microsystems operating with limited biological material ($\sim 10^3$ – 10^4 cells) and *in vivo* macrosystems with cell numbers orders of magnitude higher ($\sim 10^9$ cells), resulting in off-target allometric when considering the amount of medium required for cell culture and in applications such as hosting small liver metastases [15, 21].

Traditional fabrication techniques for OOC are often complex, multi-step, and hard to reproduce *in situ*. The culture of 3D tissues is still one of the most challenging tasks of tissue engineering, and many vascularization approaches are being investigated [86, 87]. Specifically, the culture of primary hepatocytes is challenging due to its relatively high metabolic rate, leading to diffusion barrier length of 30–100 μ m [88] and requiring a very dense vascular network for efficient oxygen delivery *in vivo*. Some strategies focus on the perfusion system itself and thereafter relying on the embedding of tissues in gel structures. While this approach has generated significant advances and shed light on emerging properties of biological systems [10, 86], the use of matrices inherently limits the amount of post-mitotic cells that can be introduced due to the lack of dense vasculature

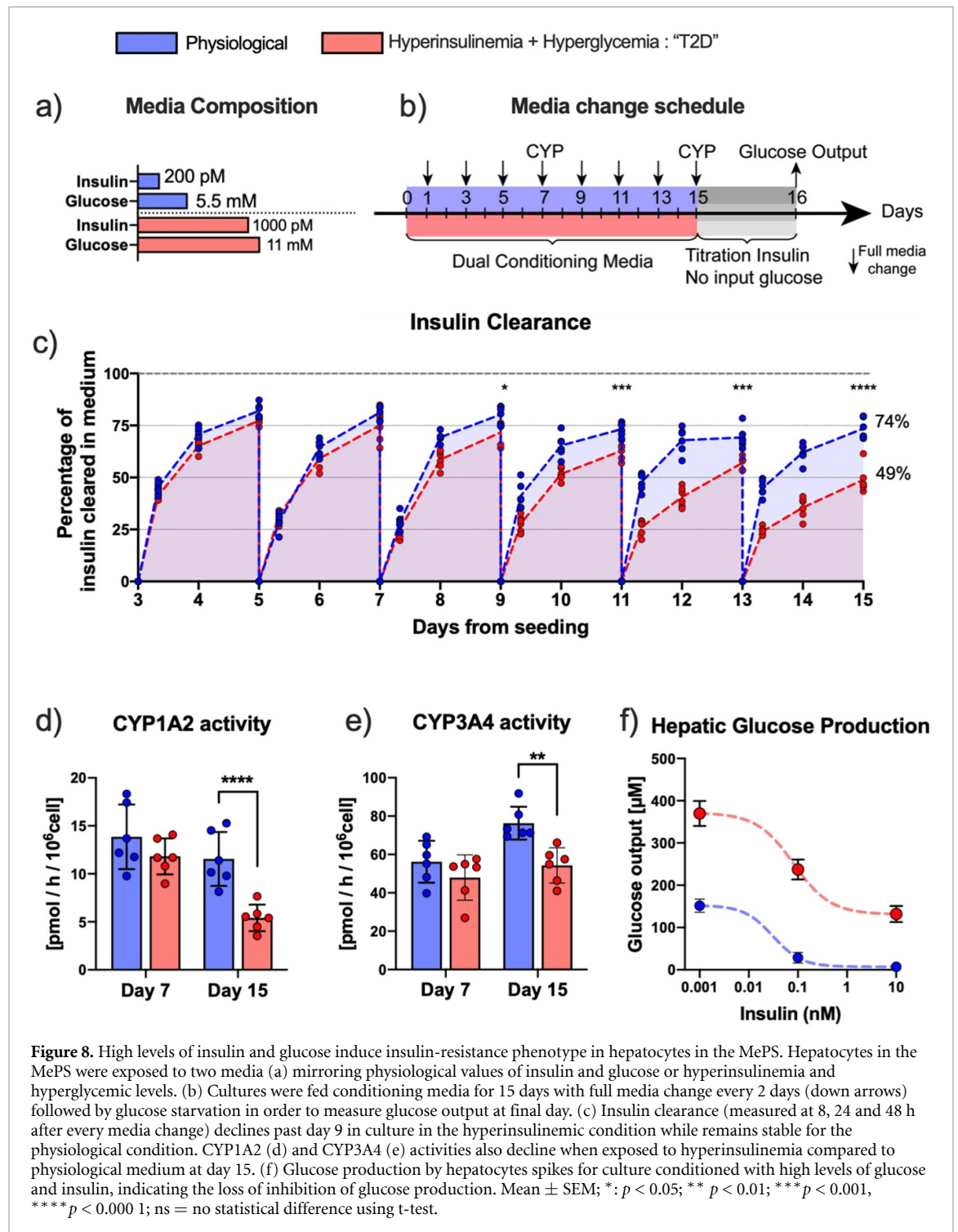


Figure 8. High levels of insulin and glucose induce insulin-resistance phenotype in hepatocytes in the MePS. Hepatocytes in the MePS were exposed to two media (a) mirroring physiological values of insulin and glucose or hyperinsulinemia and hyperglycemic levels. (b) Cultures were fed conditioning media for 15 days with full media change every 2 days (down arrows) followed by glucose starvation in order to measure glucose output at final day. (c) Insulin clearance (measured at 8, 24 and 48 h after every media change) declines past day 9 in culture in the hyperinsulinemic condition while remains stable for the physiological condition. CYP1A2 (d) and CYP3A4 (e) activities also decline when exposed to hyperinsulinemia compared to physiological medium at day 15. (f) Glucose production by hepatocytes spikes for culture conditioned with high levels of glucose and insulin, indicating the loss of inhibition of glucose production. Mean \pm SEM; *: $p < 0.05$; ** $p < 0.01$; *** $p < 0.001$, **** $p < 0.0001$; ns = no statistical difference using t-test.

at the time of seeding. In this work, our approach was inspired by hollow fiber bioreactors, and we focused on the fabrication and implementation of scaffolds with pre-existing vascular-like networks to provide nutrients and oxygen efficiently to the cells while shielding them from damaging shear.

Even though the field of OOC has provided numerous new methods for 3D culture, only a few options have been commercially successful [79, 80]. Two major challenges facing these emerging technologies are the cost of production and the need

to establish reproducible, user-friendly protocols [89, 90]. In this work, we showed that the $P\mu$ SLA was a useful manufacturing technique to create biological scaffolds for 3D culture. Compared to traditional SLA techniques working in a point-by-point fashion, the $P\mu$ SLA cures materials in a layer-by-layer manner, therefore dramatically increasing the manufacturing speed while conserving micrometric resolution and allowing the complete fabrication of MePS within only 3 h. The field of 3D printing is a rapidly growing discipline with commercial printers constantly

evolving, and with the rise of new technologies such as holographic volumetric 3D printing [91], we speculate that even more rapid printing of MePS will be achieved in the future. Furthermore, in addition to only requiring off-the-shelf material for the fabrication, all post-printing processes were developed to be performed batchwise in solution at room temperature, therefore ensuring sterility and preventing failing points in traditional microfluidics such as the formation of bubbles and tearing of the microchannels by manual handling [90].

Careful design of the material chemistry allowed the creation of nanopores for increased oxygen exchange between the fluidic and cellular compartments. The resulting material also featured relatively high elasticity with a Young's modulus of 310 kPa: harder than typical hydrogels made with bioprinters but softer than hard polymers used in commercial 3D printers. Although SLA has been reported to fabricate materials with Young's moduli as low as 420 Pa [48], these resulting hydrogels typically swell once put in isotonic solutions which was also observed when we replaced our monomer (HDDA 226 MW) with a monomer of higher molecular weight (polyethylene glycol dimethyl acrylate, 750 MW) as the material underwent swelling once put in PBS (data not shown), therefore deforming critical microfeatures of the 3D MePS.

In this work, we capitalized on the already existing Liverchip[®] as an attractive perfusion device for our system, as the recirculating motion of the media allowed for small operating volumes at robust flow rates. The cell culture method used here has several practical and fundamental advantages that distinguish it from other OOC devices. The recirculation of a low volume medium (1.4 ml) with respect to the number of cells (1×10^6) reaches levels closer to physiological values than other devices. Furthermore, the absorption of biological compounds to lipophilic materials used for MPS fabrication, such as PDMS [92], can dramatically alter experimental interpretations. Our photopolymerizable material and bioinert bioreactor avoid such issues (see figure S9).

The optimization of the MePS design via numerical simulations allowed the generation of 3D structures that could operate despite small fabrication defects inherent to any manufacturing methods. We focused on the oxygenation and shear forces experienced by the tissue as the two critical parameters working against each other but were critical for liver function and viability [93, 94]. This approach permitted the prediction of the ideal range of flow rates and the scaffold geometry adjustment. The MePS behaves like hollow fibers in a bioreactor, but with a capillary density close to the diffusion limit of oxygen ($\sim 120 \mu\text{m}$). Nonetheless, conversely to hollow fibers made of highly permeable materials, our 3D printed material was not permissive enough for complete oxygenation of the tissue, therefore requiring the

fabrication of lateral windows to artificially increase mass transfer. While the windows accounted for 23% of the total surface area of the scaffold, the numerical simulations only predicted an interstitial flow of 13.8% in the worst case scenario, which was only possible due to the nonlinear dependency between hydraulic diameter D_H and hydraulic resistance R_H ($R_H \sim 1/D_H^4$) [95].

The biological characterization of the hepatocytes cultured in the MePS showed improved health and function compared to the commercial PSs made of hollow microconduits. The quantification of dsDNA in the MePS, which was previously reported to correlate with cell content in culture [61], indicated that most of the 1×10^6 cells introduced in our system remained after 7 days of culture ($>82\%$ of total cells seeded). The direct measurement of OCR revealed that the hepatocytes in the MePS consumed more oxygen over time, from 52 at day 1–94 amol/cell/s at day 7, within the reported range 10–120 amol/cell/s previously reported for primary hepatocytes [26, 96], which indicated that the culture increased its metabolic activity. The cells in the MePS released low levels of cytosolic enzymes (ALT and LDH), similar to values in the PS scaffolds, confirming that they retained high levels of viability throughout the operation of the cell culture. Low levels of these cytosolic enzymes in the cell culture medium have previously been correlated with low hepatocyte death [97]. The cells in the MePS also presented elevated ureagenesis and albumin secretion in comparison to the PS system indicating increased hepatic activity. Furthermore, sustained albumin secretion was achieved from day 9 to day 21. The activity of the CYP450 enzymes CYP1A2 and CYP3A4 also was higher in the MePS compared to the PS scaffolds, indicating elevated metabolic activity of the tissue. The analysis of cytokine secretion in the MePS showed reduced secretion of cytokines, notably the decreased secretion of IL-8 which has previously been reported to alter the production of acute phase protein in hepatocytes *in vitro* [98].

The low release of cytotoxic markers, the increased oxygen consumption by the cells, the elevated secretion of urea and albumin, and the increased activity of cytochrome P450 enzymes in the MePS compared to the MPS indicate that the tissues behave differently at a cellular level. Several features of the MePS may contribute to these differences. First, the median shear stress predicted in the MePS (0.9 mPa) was significantly lower than in the MPS (1.6 mPa). While the field has established the detrimental effects of excessive shear forces above 500 mPa [20], the data linking a lower range of shear stress and hepatic function has been inconsistent, due in part to different culture formats, model interpretations, or donor variability, with some studies showing a beneficial effect of shear on hepatocytes at low values (<33 mPa) [43, 97, 99]. Second, the predicted oxygen tensions in the MePS and the PS scaffolds were

drastically different, with median values of 10.1 kPa and 16.2 kPa, respectively, which could support the idea that physiological tension levels could contribute to the phenotypic difference observed between the two systems. Great advances have been made in understanding the role of oxygen gradients in hepatic function *in vivo* through hepatic zonation [33], but *in vitro* data are still inconclusive regarding the optimal oxygen tension required within the tissue for a culture format [100]. While some successful cultures of primary hepatocytes require culture at 95% oxygen saturation (~ 96 kPa) [101], more recent studies [102] have shown a deleterious effect of an excess of oxygen with regard to hepatocyte dedifferentiation and obtained healthier culture at physiological levels of oxygen tension (5 kPa). We suspect that a critical aspect to elucidate these contradicting facts was to account for the active transport of oxygen to the tissue, and that oxygen tension at the cellular level was more informative than the oxygen input of the system. Third, the scaffold design fosters favorable cell–cell contacts such as those known to promote liver function [103]. Local cell density and accumulation of autocrine factors may also contribute.

Owing to the tissue's mesoscopic scale in our MePS and its elevated metabolic activity, we replicated *in vitro* some clinical features of T2D as a proof of concept that the MePS can be used to study metabolic disorders physiologically and quantitatively. Type 2 diabetes is a complex multisystemic disease characterized by insulin resistance in which multiple organs come into play, leading to the overproduction of insulin at a basal level [104]. T2D has also been associated with metabolic syndrome defined in part by hyperglycemia, which can be used to predict T2D onset. While canonical culture media for primary hepatic culture generally contain extremely high concentrations of insulin and glucose compared to physiological levels, we wanted to test the hypothesis that cells in our culture system would respond differently when exposed to either physiological or T2D levels of insulin and glucose. When exposed to physiological medium, the cells had a stable phenotype regarding insulin clearance, cytochrome P450 activities, and glucose output. However, when exposed to hyperglycemic and hyperinsulinemic levels over the course of 15 days, the cells in the MePS started to deviate from the physiological condition from day 9, exhibiting a drop of insulin clearance from 74% to 49% and a complete loss of gluconeogenesis inhibition at high level of insulin.

5. Conclusions

This work reports, to the best of our knowledge, the first long-term culture of primary hepatocytes at mesoscale in a 3D printed scaffold. The fabrication of the MePS at high-throughput was made possible by

projection micro-stereolithography capable of printing centimetric scaffolds with micrometric resolution. The design of the MePS allows an even distribution of flow throughout the scaffold for the enhanced delivery of oxygen and other nutrients to the cellular compartment. The liver culture in our system features elevated albumin and urea synthesis, CYP activity, and low inflammation profile over 21 days. This model can establish chronic insulin-resistant culture for the study of metabolic disorders *in vitro* at scales closer to *in vivo* samples. Furthermore, by decoupling the perfusion system to its scaffold, the MePS can be scaled from its functional unit and be integrated into various human-on-chip platforms to interact with multiple organs. We believe that mesoscopic physiological systems will help to bridge the gap between *in vitro* MPS and *in vivo* animal models by improving the scaling of tissue culture. Future work will include the co-culture of hepatocytes with resident immune cells to elucidate inflammation mechanisms during type 2 diabetes onset.

Data availability statement

All data that support the findings of this study are included within the article (and any supplementary files).

Acknowledgments

This research was sponsored by NIH R01EB010246, NIH UH2TR000496, NIH T32GM008334, NIH T32-ES007020, the DARPA Microphysiological Systems Program (W911NF-12-2-0039) and NovoNordisk. We are grateful to the Institute for Soldier Nanotechnologies and Whitehead Institute for access to their core facilities. We are also grateful to Collin Edington, Kelly Chen, Jason Velasquez, David Trumper, Jacob Jeppesen and Jessica Ungerleider for their helpful discussion and technical assistance.


Contribution

PS, MSR, HL, NF: hardware design, testing and troubleshooting. PS, MSR, NE, PH: material design and testing. PS: computational modeling. PS: experimental execution. PS: cell culture. PS, AW: data analysis. PS, MSR: figures and tables configuration. PS, MSR, AW, NE, LGG: writing. LGG, NF: supervision.

All authors commented and approved the manuscript.

ORCID iDs

Pierre Sphabmixay  <https://orcid.org/0000-0003-0119-9173>

Micha Sam Brickman Raredon  <https://orcid.org/0000-0003-1441-6122>

Alex J-S Wang  <https://orcid.org/0000-0001-6005-6901>
 Howon Lee  <https://orcid.org/0000-0001-5778-2398>
 Paula T Hammond  <https://orcid.org/0000-0002-9835-192X>
 Nicholas X Fang  <https://orcid.org/0000-0001-5713-629X>
 Linda G Griffith  <https://orcid.org/0000-0002-1801-5548>

References

- [1] Ahadian S *et al* 2017 Organ-on-a-chip platforms: a convergence of advanced materials, cells, and microscale technologies *Adv. Healthcare Mater.* **7** 1700506–53
- [2] Elliott N T and Yuan F 2011 A review of three-dimensional *in vitro* tissue models for drug discovery and transport studies *J. Pharm. Sci.* **100** 59–74
- [3] Folkman J and Hochberg M 1973 Self-regulation of growth in three dimensions *J. Exp. Med.* **7** 1–9
- [4] Wikswo J P 2014 The relevance and potential roles of microphysiological systems in biology and medicine *Exp. Biol. Med.* **239** 1061–72
- [5] Sharma V and McNeill J H 2009 To scale or not to scale: the principles of dose extrapolation *Br. J. Pharmacol.* **157** 907–21
- [6] Domansky K, Inman W, Serdy J, Dash A, Lim M H M and Griffith L G 2010 Perfused multiwell plate for 3D liver tissue engineering *Lab Chip* **10** 51–58
- [7] Huh D, Hamilton G A and Ingber D E 2011 From 3D cell culture to organs-on-chips *Trends Cell Biol.* **21** 745–54
- [8] Huh D, Matthews B D, Mammoto A, Montoya-Zavala M, Hsin H Y and Ingber D E 2010 Reconstituting organ-level lung functions on a chip *Science* **328** 1662–8
- [9] Chang S-Y *et al* 2017 Human liver-kidney model elucidates the mechanisms of aristolochic acid nephrotoxicity *JCI Insight* **2** 22
- [10] Osaki T, Sivathanu V and Kamm R D 2018 Engineered 3D vascular and neuronal networks in a microfluidic platform *Sci. Rep.* **8** 5168
- [11] Chen M B, Hajal C, Benjamin D C, Yu C, Azizgolshani H, Hynes R O and Kamm R D 2018 Inflamed neutrophils sequestered at entrapped tumor cells via chemotactic confinement promote tumor cell extravasation *Proc. Natl Acad. Sci. USA* **115** 7022–7
- [12] Shin Y, Choi S H, Kim E, Bylykbashi E, Kim J A, Chung S, Kim D Y, Kamm R D and Tanzi R E 2019 Blood–brain barrier dysfunction in a 3D *in vitro* model of Alzheimer’s disease *Adv. Sci.* **6** 1900962
- [13] Ronaldson-Boucharde K *et al* 2019 Engineering of human cardiac muscle electromechanically matured to an adult-like phenotype *Nat. Protoc.* **14** 2781–817
- [14] Zhang J *et al* 2021 Primary human colonic mucosal barrier crosstalk with super oxygen-sensitive *faecalibacterium prausnitzii* in continuous culture *Med* **2** 74–98.e9
- [15] Edington C D, Cirit M, Chen W L K, Clark A M, Wells A, Trumper D L and Griffith L G 2017 Integration of systems biology with organs-on-chips to humanize therapeutic development *Microfluidics, BioMEMS, and Medical Microsystems XV* vol 10061 (<https://doi.org/10.1117/12.2256078>)
- [16] Edington C D *et al* 2018 Interconnected microphysiological systems for quantitative biology and pharmacology studies *Sci. Rep.* **8** 4530
- [17] McAleer C W *et al* 2019 Multi-organ system for the evaluation of efficacy and off-target toxicity of anticancer therapeutics *Sci. Transl. Med.* **11** eaav1386
- [18] Trapecar M *et al* 2020 Gut-liver physiomechanics reveal paradoxical modulation of IBD-related inflammation by short-chain fatty acids *Cell Syst.* **10** 223–239.e9
- [19] Downen J M *et al* 2014 Control of cell identity genes occurs in insulated neighborhoods in mammalian chromosomes *Cell* **159** 374–87
- [20] Clark A M *et al* 2014 A microphysiological system model of therapy for liver micrometastases *Exp. Biol. Med.* **239** 1170–9
- [21] Clark A M, Ma B, Taylor D L, Griffith L and Wells A 2016 Liver metastases: microenvironments and *ex-vivo* models *Exp. Biol. Med.* **241** 1639–52
- [22] Xiang C *et al* 2019 Long-term functional maintenance of primary human hepatocytes *in vitro* *Science* **364** 399–402
- [23] Zeilinger K, Freyer N, Damm G, Seehofer D and Knöspel F 2016 Cell sources for *in vitro* human liver cell culture models *Exp. Biol. Med.* **241** 1684–98
- [24] Zhang S, Chen L, Liu T, Wang Z and Wang Y 2013 Integration of single-layer skin hollow fibers and scaffolds develops a three-dimensional hybrid bioreactor for bioartificial livers *J. Mater. Sci. Mater. Med.* **25** 207–16
- [25] Bachmann A *et al* 2015 3D cultivation techniques for primary human hepatocytes *Microarrays* **4** 64–83
- [26] Khakpour S, Di Renzo A, Curcio E, Di Maio F P, Giorno L and De Bartolo L 2017 Oxygen transport in hollow fibre membrane bioreactors for hepatic 3D cell culture. A parametric study *J. Memb. Sci.* **544** 312–22
- [27] Long T J, Cosgrove P A, Dunn R T, Stolz D B, Hamadeh H, Afshari C, McBride H and Griffith L G 2016 Modeling therapeutic antibody-small molecule drug-drug interactions using a three-dimensional perfusable human liver coculture platform *Drug Metabol. Dispos.* **44** 1940–8
- [28] Clark A M, Kumar M P, Wheeler S E, Young C L, Venkataraman R, Stolz D B, Griffith L G, Lauffenburger D A and Wells A 2018 A model of dormant-emergent metastatic breast cancer progression enabling exploration of biomarker signatures *Mol. Cell Proteomics* **17** 619–30
- [29] Ortega-Prieto A M *et al* 2018 3D microfluidic liver cultures as a physiological preclinical tool for hepatitis B virus infection *Nat. Commun.* **9** 682
- [30] Kostrzewski T, Cornforth T, Snow S A, Ouro-Gnao L, Rowe C, Large E M and Hughes D J 2017 Three-dimensional perfused human *in vitro* model of non-alcoholic fatty liver disease *World J. Gastroenterol.: WJG* **23** 204–13
- [31] Rubiano A *et al* 2021 Characterizing the reproducibility in using a liver microphysiological system for assaying drug toxicity, metabolism, and accumulation *Clin. Transl. Sci.* **14** 1049–61
- [32] Ebrahimkhani M R, Neiman J A S, Raredon M S B, Hughes D J and Griffith L G 2014 Bioreactor technologies to support liver function *in vitro* *Adv. Drug Deliv. Rev.* **69** 132–57
- [33] Godoy P *et al* 2013 Recent advances in 2D and 3D *in vitro* systems using primary hepatocytes, alternative hepatocyte sources and non-parenchymal liver cells and their use in investigating mechanisms of hepatotoxicity, cell signaling and ADME *Arch. Toxicol.* **87** 1315–530
- [34] Kamada T, Hayashi N, Sato N, Kasahara A and Abe H 1986 Estimated hepatic oxygen consumption in patients with chronic liver diseases as assessed by organ reflectance spectrophotometry *Dig. Dis. Sci.* **31** 119–24
- [35] Inman W, Domansky K, Serdy J, Owens B, Trumper D and Griffith L G 2007 Design, modeling and fabrication of a constant flow pneumatic micropump *J. Microeng. Microeng.* **17** 891–9
- [36] Powers M J *et al* 2002 A microfabricated array bioreactor for perfused 3D liver culture *Biotechnol. Bioeng.* **78** 257–69
- [37] Powers M J, Janigian D M, Wack K E, Baker C S, Stolz D B and Griffith L G 2002 Functional behavior of primary rat liver cells in a three-dimensional perfused microarray bioreactor *Tissue Eng.* **8** 499–513

- [38] Sivaraman A, Leach J K, Townsend S, Iida T, Hogan B J, Stolz D B, Fry R, Samson L D, Tannenbaum S R and Griffith L G 2005 A microscale *in vitro* physiological model of the liver: predictive screens for drug metabolism and enzyme induction *Curr. Drug Metab.* **6** 569–91
- [39] Hwa A J, Fry R C, Sivaraman A, So P T, Samson L D, Stolz D B and Griffith L G 2007 Rat liver sinusoidal endothelial cells survive without exogenous VEGF in 3D perfused co-cultures with hepatocytes *FASEB J.* **21** 2564–79
- [40] Marson A *et al* 2008 Connecting microRNA genes to the core transcriptional regulatory circuitry of embryonic stem cells *Cell* **134** 521–33
- [41] Sun C, Fang N, Wu D M and Zhang X 2005 Projection micro-stereolithography using digital micro-mirror dynamic mask *Sens. Actuators A* **121** 113–20
- [42] Xia C and Fang N X 2009 3D microfabricated bioreactor with capillaries *Biomed. Microdevices* **11** 1309–15
- [43] Kan P, Miyoshi H, Yanagi K and Ohshima N 1998 Effects of shear stress on metabolic function of the co-culture system of hepatocyte/nonparenchymal cells for a bioartificial liver *ASAIO J. KW* **44** M441–M444
- [44] Ledezma G A, Folch A, Bhatia S N, Balis U J, Yarmush M L and Toner M 1999 Numerical model of fluid flow and oxygen transport in a radial-flow microchannel containing hepatocytes *J. Biomech. Eng.* **121** 58–64
- [45] Park J, Li Y, Berthiaume F, Toner M, Yarmush M L and Tilles A W 2008 Radial flow hepatocyte bioreactor using stacked microfabricated grooved substrates *Biotechnol. Bioeng.* **99** 455–67
- [46] Consolo F, Fiore G B, Truscillo S, Caronna M, Morbiducci U, Montevecchi F M and Redaelli A 2009 A computational model for the optimization of transport phenomena in a rotating hollow-fiber bioreactor for artificial liver *Tissue Eng.* **15** 41–55
- [47] Podichetty J T, Bhaskar P R, Singarapu K and Madihal S V 2014 Multiple approaches to predicting oxygen and glucose consumptions by HepG2 cells on porous scaffolds in an axial-flow bioreactor *Biotechnol. Bioeng.* **112** 393–404
- [48] Zhang B *et al* 2016 Biodegradable scaffold with built-in vasculature for organ-on-a-chip engineering and direct surgical anastomosis *Nat. Mater.* **15** 669–78
- [49] Melchels F P W, Feijen J and Grijpma D W 2010 A review on stereolithography and its applications in biomedical engineering *Biomaterials* **31** 6121–30
- [50] Lee H and Fang N X 2012 Micro 3D printing using a digital projector and its application in the study of soft materials mechanics *J. Vis. Exp.* **69** e4457
- [51] Espinosa-Hoyos D, Jagielska A, Homan K A, Du H, Busbee T, Anderson D G, Fang N X, Lewis J A and Van Vliet K J 2018 Engineered 3D-printed artificial axons *Sci. Rep.* **8** 478
- [52] Kaplowitz N 2005 Idiosyncratic drug hepatotoxicity *Nat. Rev. Drug Discov.* **4** 489–99
- [53] Tagle D A 2019 The NIH microphysiological systems program: developing *in vitro* tools for safety and efficacy in drug development *Curr. Opin. Pharmacol.* **48** 146–54
- [54] Esch M B, Prot J-M, Wang Y I, Miller P, Llamas-Vidales J R, Naughton B A, Applegate D R and Shuler M L 2018 Multi-cellular 3D human primary liver cell culture elevates metabolic activity under fluidic flow *Lab Chip* **15** 2269–77
- [55] Hoffmann S A, Muller-Vieira U, Biemel K, Knobloch D, Heydel S, Lubberstedt M, Nussler A K, Andersson T B, Gerlach J C and Zeilinger K 2012 Analysis of drug metabolism activities in a miniaturized liver cell bioreactor for use in pharmacological studies *Biotechnol. Bioeng.* **109** 3172–81
- [56] Wardwell-Swanson J *et al* 2020 A framework for optimizing high-content imaging of 3D models for drug discovery *SLAS Discov.* **25** 709–22
- [57] Loomba R and Sanyal A J 2013 The global NAFLD epidemic *Nat. Rev. Gastroenterol. Hepatol.* **10** 686–90
- [58] Dewidar B, Kahl S, Pafili K and Roden M 2020 Metabolic liver disease in diabetes—from mechanisms to clinical trials *Metabolism* **111** 154299
- [59] Wisse E, Braet F, Luo D, De Zanger R, Jans D, Crabbe E and Vermoesen A 1996 Structure and function of sinusoidal lining cells in the liver *Toxicol. Pathol.* **24** 100–11
- [60] Ge Q, Sakhaei A H, Lee H, Dunn C K, Fang N X and Dunn M L 2016 Multimaterial 4D printing with tailorable shape memory polymers *Sci. Rep.* **6** 31110
- [61] Otto W R 2005 Fluorimetric DNA assay of cell number *Epidermal Cells: Methods and Protocols* ed K Turksen (Totowa, NJ: Humana Press) pp 251–62
- [62] Ungerleider J, Sphabmixay P, Jeppesen J and Griffith L 3D *in vitro* models of hepatic insulin resistance (Manuscript in preparation)
- [63] Heller M J and Guttman A 2001 *Integrated Microfabricated Bioelectronics* (Boca Raton, FL: CRC Press)
- [64] Yeh W-C, Li P-C, Jeng Y-M, Hsu H-C, Kuo P-L, Li M-L, Yang P-M and Lee P H 2002 Elastic modulus measurements of human liver and correlation with pathology *Ultrasound Med. Biol.* **28** 467–74
- [65] Brydson J A 1999 16—plastics based on styrene *Plastics Materials* 7th edn, ed J A Brydson (Oxford: Butterworth-Heinemann) pp 425–65
- [66] Woo K M, Chen V J and Ma P X 2003 Nano-fibrous scaffolding architecture selectively enhances protein adsorption contributing to cell attachment *J. Biomed. Mater. Res. A* **67** 531–7
- [67] Zhang L and Webster T J 2009 Nanotechnology and nanomaterials: promises for improved tissue regeneration *Nano Today* **4** 66–80
- [68] Casillo S M, Peredo A P, Perry S J, Chung H H and Gaboriski T R 2017 Membrane pore spacing can modulate endothelial cell–substrate and cell–cell interactions *ACS Biomater. Sci. Eng.* **3** 243–8
- [69] Sun M, Han K, Hu R, Liu D, Fu W and Liu W 2021 Advances in micro/nanoporous membranes for biomedical engineering *Adv. Healthcare Mater.* **10** 2001545
- [70] Gao Y, Baca A M, Wang B and Ogilby P R 2015 Activation barriers for oxygen diffusion in polystyrene and polycarbonate glasses: effects of low molecular weight additives *Macromolecules* **27** 7041–48
- [71] Ko J, Cho K, Han S W, Sung H K, Baek S W, Koh W-G and Yoon J S 2017 Hydrophilic surface modification of poly(methyl methacrylate)-based ocular prostheses using poly(ethylene glycol) grafting *Colloids Surf. B* **158** 287–94
- [72] Kietzmann T 2017 Metabolic zonation of the liver: the oxygen gradient revisited *Redox Biol.* **11** 622–30
- [73] Jeschke M G, Klein D, Thasler W E, Bolder U, Schlitt H J, Jauch K W and Weiss T S 2008 Insulin decreases inflammatory signal transcription factor expression in primary human liver cells after LPS challenge *Mol. Med.* **14** 11–19
- [74] Van De Kerkhove M P, Poock P P, Van Wijk A C, Galavotti D, Hoekstra R, Van Gulik T M and Chamuleau R A 2005 Assessment and improvement of liver specific function of the AMC-bioartificial liver *Int. J. Artif. Organs.* **28** 617–30
- [75] Freyer N, Knöspel F, Damm G, Greuel S, Schneider C, Seehofer D, Stöhr T, Petersen K-U and Zeilinger K 2019 Metabolism of remimazolam in primary human hepatocytes during continuous long-term infusion in a 3D bioreactor system *Drug Des. Devel. Ther.* **13** 1033–47
- [76] Levitt D and Levitt M 2016 Human serum albumin homeostasis: a new look at the roles of synthesis, catabolism, renal and gastrointestinal excretion, and the clinical value of serum albumin measurements *Int. J. Gen. Med.* **9** 229–55
- [77] Mizoi K, Hosono M, Kojima H and Ogihara T 2020 Establishment of a primary human hepatocyte spheroid system for evaluating metabolic toxicity using dacarbazine

- under conditions of CYP1A2 induction *Drug Metab. Pharmacokinet.* **35** 201–6
- [78] Zanger U M and Schwab M 2013 Cytochrome P450 enzymes in drug metabolism: regulation of gene expression, enzyme activities, and impact of genetic variation *Pharmacol. Ther.* **138** 103–41
- [79] Hussain T, Al-Attas O S, Al-Daghri N M, Mohammed A A, De Rosas E, Ibrahim S, Vinodson B, Ansari M G and El-Din K I 2014 Induction of CYP1A1, CYP1A2, CYP1B1, increased oxidative stress and inflammation in the lung and liver tissues of rats exposed to incense smoke *Mol. Cell. Biochem.* **391** 127–36
- [80] Hwang J-C et al 2021 Immobilization stress increased cytochrome P450 1A2 (CYP1A2) expression in the ovary of rat *J. Animal. Reproduct. Biotechnol.* **36** 9–16
- [81] Hunter P 2012 The inflammation theory of disease *EMBO Rep.* **13** 968–70
- [82] Robinson M W, Harmon C and Farrelly C O R 2016 Liver immunology and its role in inflammation and homeostasis *Cell. Mol. Immunol.* **13** 267–76
- [83] Hameed I, Masoodi S R, Mir S A, Nabi M, Ghazanfar K and Ganai B A 2015 Type 2 diabetes mellitus: from a metabolic disorder to an inflammatory condition *World J. Diabetes* **6** 598–16
- [84] Song S H, McIntyre S S, Shah H, Veldhuis J D, Hayes P C and Butler P C 2000 Direct measurement of pulsatile insulin secretion from the portal vein in human subjects *J. Clin. Endocrinol. Metab.* **85** 4491–9
- [85] Sindelar D K, Chu C A, Venson P, Donahue E P, Neal D W and Cherrington A D 1998 Basal hepatic glucose production is regulated by the portal vein insulin concentration *Diabetes* **47** 523–9
- [86] Osaki T, Sivathanu V and Kamm R D 2018 ScienceDirect Vascularized microfluidic organ-chips for drug screening, disease models and tissue engineering *Curr. Opin. Biotechnol.* **52** 116–23
- [87] Nashimoto Y et al 2017 Integrating perfusable vascular networks with a three-dimensional tissue in a microfluidic device *Integr. Biol.* **9** 506–18
- [88] Place T L, Domann F E and Case A J 2017 Limitations of oxygen delivery to cells in culture: an underappreciated problem in basic and translational research *Free Radic. Biol. Med.* **113** 311–22
- [89] Franzen N, Van Harten W H, Retèl V P, Loskill P, Van Den Eijnden-van Raaij J and Jzerman M I 2019 Impact of organ-on-a-chip technology on pharmaceutical R&D costs *Drug Discov. Today* **24** 1720–4
- [90] Low L A and Tagle D A 2017 Organs-on-chips: progress, challenges, and future directions *Exp. Biol. Med.* **242** 1573–8
- [91] Siltanen C, Diakataou M, Lowen J, Haque A, Rahimian A, Stybayeva G and Revzin A 2017 One step fabrication of hydrogel microcapsules with hollow core for assembly and cultivation of hepatocyte spheroids *Acta Biomater.* **50** 428–36
- [92] Li N, Schwartz M and Ionescu-Zanetti C 2009 PDMS compound adsorption in context *J. Biomol. Screen.* **14** 194–202
- [93] Tilles A W, Baskaran H, Roy P, Yarmush M L and Toner M 2001 Effects of oxygenation and flow on the viability and function of rat hepatocytes cocultured in a microchannel flat-plate bioreactor *Biotechnol. Bioeng.* **73** 379–89
- [94] Tanaka Y, Yamato M, Okano T, Kitamori T and Sato K 2006 Evaluation of effects of shear stress on hepatocytes by a microchip-based system *Meas. Sci. Technol.* **17** 3167–70
- [95] White F 2015 *Fluid Mechanics* 8th edn (London: McGraw-Hill Education)
- [96] Mareels G, Poyck P P C, Eloot S, Chamuleau R A F M and Verdonck P R 2006 Three-dimensional numerical modeling and computational fluid dynamics simulations to analyze and improve oxygen availability in the AMC bioartificial liver *Ann. Biomed. Eng.* **34** 1729–44
- [97] Esch M B, Mahler G J, Stokol T and Shuler M L 2014 Body-on-a-chip simulation with gastrointestinal tract and liver tissues suggests that ingested nanoparticles have the potential to cause liver injury *Lab Chip* **14** 3081–92
- [98] Wigmore S J, Fearon K C H, Maingay J P, Lai P B S and Ross J 1997 Interleukin-8 can mediate acute-phase protein production by isolated human hepatocytes *Am. Physiol. Soc.* **273** E720–6
- [99] Tatosian D A and Shuler M L 2009 A novel system for evaluation of drug mixtures for potential efficacy in treating multidrug resistant cancers *Biotechnol. Bioeng.* **103** 187–98
- [100] Ehrlich A, Duche D, Ouedraogo G and Nahmias Y 2019 Challenges and opportunities in the design of liver-on-chip microdevices *Annu. Rev. Biomed. Eng.* **21** 219–39
- [101] Kidambi S, Yarmush R S, Novik E, Chao P, Yarmush M L and Nahmias Y 2009 Oxygen-mediated enhancement of primary hepatocyte metabolism, functional polarization, gene expression, and drug clearance *Proc. Natl Acad. Sci. USA* **106** 15714–9
- [102] Guo R, Xu X, Lu Y and Xie X 2017 Physiological oxygen tension reduces hepatocyte dedifferentiation in *in vitro* culture *Sci. Rep.* **7** 5923
- [103] Jurin R R and McCune S A 1985 Effect of cell density on metabolism in isolated rat hepatocytes *J. Cell. Physiol.* **123** 442–8
- [104] DeFronzo R A et al 2015 Type 2 diabetes mellitus *Nat. Rev. Dis. Primers.* **23** 15019